Origins of a Relatively Tight Lower Bound on Anthropogenic Aerosol Radiative Forcing from Bayesian Analysis of Historical Observations

ANNA LEA ALBRIGHT,[a] CRISTIAN PROISTOSESCU,[b] AND PETER HUYBERS[c]

[a] *Laboratoire de Météorologique Dynamique, Sorbonne Université, École Normale Supérieure, École Polytechnique, Paris*
[b] *Department of Atmospheric Sciences and Department of Geology, University of Illinois at Urbana–Champaign, Champaign, Illinois*
[c] *Department of Earth and Planetary Sciences, Harvard University, Cambridge, Massachusetts*

(Manuscript received 26 February 2021, in final form 4 August 2021)

ABSTRACT: A variety of empirical estimates have been published for the lower bounds on aerosol radiative forcing, clustered around -1.0 or $-2.0\,\mathrm{W\,m^{-2}}$. The reasons for obtaining such different constraints are not well understood. In this study, we explore bounds on aerosol radiative forcing using a Bayesian model of aerosol forcing and Earth's multi-time-scale temperature response to radiative forcing. We first demonstrate the ability of a simple aerosol model to emulate aerosol radiative forcing simulated by 10 general circulation models. A joint inference of climate sensitivity and effective aerosol forcing from historical surface temperatures is then made over 1850–2019. We obtain a maximum likelihood estimate of aerosol radiative forcing of $-0.85\,\mathrm{W\,m^{-2}}$ (5%–95% credible interval from -1.3 to $-0.50\,\mathrm{W\,m^{-2}}$) for 2010–19 relative to 1750 and an equilibrium climate sensitivity of 3.4°C (5%–95% credible interval from 1.8° to 6.1°C). The wide range of climate sensitivity reflects difficulty in empirically constraining long-term responses using historical temperatures, as noted elsewhere. A relatively tight bound on aerosol forcing is nonetheless obtained from the structure of temperature and aerosol precursor emissions and, particularly, from the rapid growth in emissions between 1950 and 1980. Obtaining a 5th percentile lower bound on aerosol forcing around $-2.0\,\mathrm{W\,m^{-2}}$ requires prescribing internal climate variance that is a factor of 5 larger than the CMIP6 mean and assuming large, correlated errors in global temperature observations. Ocean heat uptake observations may further constrain aerosol radiative forcing but require a better understanding of the relationship between time-variable radiative feedbacks and radiative forcing.

KEYWORDS: Aerosol radiative effect; Forcing; Bayesian methods; Idealized models; Internal variability

1. Introduction

Historical aerosol forcing is a major source of uncertainty in Earth's energy budget, with attendant consequences for observation-based estimates of the transient climate response (TCR) and equilibrium climate sensitivity (ECS) (Andreae et al. 2005; Otto et al. 2013; Forster 2016; Knutti et al. 2017). The most recent comprehensive review of anthropogenic aerosol radiative forcing F_{aer} indicates a 5%–95% confidence interval from -2.0 to $-0.40\,\mathrm{W\,m^{-2}}$ relative to a preindustrial baseline (Bellouin et al. 2020, sections 10 and 11 therein). This range of F_{aer} is broadly consistent with the previous range from -1.9 to $-0.1\,\mathrm{W\,m^{-2}}$ of the Fifth Assessment Report of the Intergovernmental Panel on Climate Change (IPCC AR5; Myhre et al. 2013). The magnitude of F_{aer} is inferred from both process-based constraints and empirical constraints over the historical climate record. Process-based constraints alone, however, yield a broad 5%–95% range from -3.5 to $-0.40\,\mathrm{W\,m^{-2}}$ (Bellouin et al. 2020), and our focus is understanding empirical constraints on the lower bound of F_{aer}.

Empirical lower bounds on F_{aer} are based on the inference that more negative values would imply temperature trends over parts of the twentieth century that are inconsistent with observed warming (Bellouin et al. 2020). Specific lower bounds, however, vary across studies. In one set of studies, lower bounds cluster in the range from -1.8 to $-1.7\,\mathrm{W\,m^{-2}}$ (Aldrin et al. 2012; Skeie et al. 2014, 2018), and, in another, in the range from -1.3 to $-0.70\,\mathrm{W\,m^{-2}}$ (Andronova and Schlesinger 2001; Forest et al. 2006, 2008; Murphy et al. 2009; Libardoni and Forest 2011; Stevens 2015). The origins of these discrepant estimates of F_{aer} are not entirely clear, particularly given that the frameworks make similar assumptions regarding simplified aerosol forcing and climate response models and employ similar sampling techniques. Differences, however, may stem from multiple sources, including the formulation of the forward model, sensitivity to prior distributions, choice of global or regional historical observations, interval of analysis, representation of observational error and internal climate variability, uncertainty associated with forcing efficacy, and assumptions regarding how ocean heat content observations constrain estimates (Annan 2015; Bodman and Jones 2016; Forest 2018).

In this study we examine lower bounds on F_{aer} using estimates of global-annual historical radiative forcing and surface temperature since 1850 and simple models of aerosol forcing and of the temperature response to forcing. We first present a flexible Bayesian model formulation in section 2. In section 3 we describe the inference of a $-1.3\,\mathrm{W\,m^{-2}}$ lower bound on 2010–19 F_{aer}, and in section 4 we explore the origin of these constraints, along with prospects for further constraints based upon ocean heat uptake. Given its focus on drawing physical insight from simple models, our study can be considered to occupy a rung on the hierarchical approach to climate science (Hoskins 1983; Held 2005; Polvani et al. 2017), complementing

---

Corresponding author: Anna Lea Albright, anna-lea.albright@lmd.jussieu.fr

DOI: 10.1175/JCLI-D-21-0167.1

analyses from more comprehensive models (Pincus et al. 2016; Kretzschmar et al. 2017).

2. Bayesian model

We use a model that is an extension of the linear response framework of Proistosescu and Huybers (2017). This simple framework uses temporal Green's functions to represent the response of global-mean surface temperature and net heat uptake to an imposed radiative forcing. The model is able to emulate the joint evolution of global-average surface temperature and net heat uptake across an ensemble of general circulation models (GCMs) runs from phase 5 of the Coupled Model Intercomparison Project (CMIP5). Here we extend the model to represent the radiative forcing associated with anthropogenic aerosol and volcanic emissions in greater detail.

Some previous studies have used regionally resolved simple models to bound climate sensitivity and F_{aer} (e.g., Andronova and Schlesinger 2001; Forest et al. 2002; Skeie et al. 2014). Although using regional temperature and heat uptake trends makes use of more information, it also engenders considerable complexity that is not easily accounted for. For example, hemispheric energy balance constraints ignore variations in cross-equatorial heat transport (Skeie et al. 2014; Bellouin et al. 2020), whereas models with constant hemispheric- or zonal-mean feedbacks are unlikely to reproduce the time dependence of the net radiative feedback that is thought to be primarily controlled by east–west equatorial temperature gradients (Dong et al. 2019). Furthermore, inferences of F_{aer} and climate sensitivity were found to be sensitive to regional differences in surface temperature observational estimates (Libardoni and Forest 2011, 2013), and regional uncertainties in surface temperatures since 1850 are not yet fully quantified (Chan and Huybers 2019; Davis et al. 2019).

a. Modeled and observed temperatures

Over the historical record, the temperature response to radiative forcing is well captured by linear models (e.g., Hasselmann et al. 1993; Held et al. 2010; Geoffroy et al. 2013; Caldeira and Myhrvold 2013; Haustein et al. 2019). Proistosescu and Huybers (2017) generalized the response of these linear models as a superposition of three independent linear modes, representing the dominant eigenmodes of the climate system:

$$T_{\mathrm{forced}}(t) = \sum_{n=1}^{3}\left(\frac{\alpha_n T_{2\times}}{\tau_n F_{2\times}}\right)\exp(-t/\tau_n)\star F_{\mathrm{net}}(t). \quad (1)$$

The term $T_{2\times}$, or ECS, is the equilibrium climate response to a radiative forcing per doubling of atmospheric CO_2, $F_{2\times}$. Each mode has a response time scale τ_n and contributes a fraction α_n of the equilibrium response. The forced temperature response T_{forced} is obtained by convolving each eigenmode with the net radiative forcing F_{net} and summing across all modes. Convolution in Eq. (1) is indicated by the star, and τ_n^{-1} is a normalizing factor that makes the integral $\int_{t=o}^{t=\infty}\tau_n^{-1}\exp(-t/\tau_n)$ equal one.

Following Proistosescu and Huybers (2017), we employ three eigenmodes because fewer modes result in systematic residuals in fits to GCM simulations during initial model adjustment to increased greenhouse gas forcing, whereas additional eigenmodes do not improve the fit, as judged by a Bayesian information criterion. These three modes, moreover, correspond to annual, decadal, and centennial response times to forcing, consistent with foregoing work (e.g., Caldeira and Myhrvold 2013; Tsutsui 2017; Cummins et al. 2020; Leach et al. 2021).

We assume that the difference between observed global-annual historical temperatures T_{obs} and the forced temperature response T_{forced} is due to a combination of observational uncertainty and unforced internal variability. The difference between observations and the forced response is modeled as a multivariate Gaussian,

$$P(T_{\mathrm{forced}} - T_{\mathrm{obs}}) \sim N(0, \mathbf{\Sigma}^2), \quad (2)$$

with the covariance matrix $\mathbf{\Sigma}$ representing both internal variability and observational error:

$$\mathbf{\Sigma}^2 = \rho^{|i-j|}\sigma_{\mathrm{int}}^2 + \delta_{i,j}\sigma_{\mathrm{obs}}^2. \quad (3)$$

Internal variability, the first term on the right-hand side of Eq. (3), is represented as a first-order autoregressive, or AR1, process with autocorrelation coefficient ρ in keeping with earlier studies (e.g., Frankignoul and Hasselmann 1977; Feldstein 2000; Aldrin et al. 2012; Johansson et al. 2015). Observational uncertainty is represented as uncorrelated error by the second term on the right-hand side of Eq. (3), with $\delta_{i,j}$ equaling 1 when i equals j and 0 otherwise.

We estimate the distribution of internal climate variability using 39 CMIP6 preindustrial control simulations of detrended global-mean temperature, wherein each time series is the last 400 years of the control run (Parsons et al. 2020). Internal variability is estimated as $\sigma_{\mathrm{int}}^2 = 0.019 \pm 0.011°\mathrm{C}^2$, with values equaling the mean and standard deviation across these 39 simulations. Following Schneider and Neumaier (2001), we estimate an AR1 coefficient, $\rho = 0.57 \pm 0.16$. By way of comparison, 41 CMIP5 control simulations (Taylor et al. 2011) yield $\sigma_{\mathrm{int}}^2 = 0.017 \pm 0.014°\mathrm{C}^2$ and $\rho = 0.55 \pm 0.18$. Similarly, for the 40-member Community Earth System Model version 1 Large Ensemble (CESM1 LE) (Kay et al. 2015), we obtain $\sigma_{\mathrm{int}}^2 = 0.010 \pm 0.0019°\mathrm{C}^2$ and $\rho = 0.46 \pm 0.07$. Because the CESM1 LE includes only forced runs, we use the ensemble mean of global-annual surface temperatures as the forced component and attribute ensemble spread to internal variability. We specify ρ as a free parameter in the inversion and use these results as a point of comparison because the appropriate value is not obvious (Bodman and Jones 2016). In our inversion, we set the variance associated with internal variability equal to the CMIP6 ensemble mean, $\sigma_{\mathrm{int}}^2 = 0.019°\mathrm{C}^2$. Allowing for larger internal variability by employing the CMIP6 mean, rather than the CMIP5 or CESM1 LE mean, provides a more conservative estimate of the constraints placed on aerosol forcing by historical temperatures.

For historical temperature observations we use a version of the HadCRUT4 dataset developed by Cowtan and Way (2014) that they refer to as version 2.0. Temperature data span 1850–2019 and are referenced to a 1960–90 baseline. We use time-variable values for σ_{obs}^2, squaring the standard deviation estimated by

Cowtan and Way (2014), which decreases from 0.07°C in 1850 to 0.03°C in 2019. Using NOAA temperature observations and error estimates (Zhang et al. 2019) yields qualitatively similar results, which is unsurprising given the agreement of different temperature products in the global average. Accounting for correlated error structures within observational estimates (Morice et al. 2012; Karl et al. 2015; Cowtan et al. 2015; Chan et al. 2019; Davis et al. 2019) would increase the influence of observational error, and we discuss this possibility further in section 4c.

b. *Anthropogenic aerosol forcing model*

We follow Stevens (2015) in representing aerosol radiative forcing as a log-linear function of global-annual anthropogenic aerosol precursor emissions. We, however, extend the Stevens (2015) model to include not only SO_2 emissions, but also contributions from black carbon, B, and organic carbon, O, in units of Tg of each per year:

$$F_{\mathrm{aer}} = \alpha_{\mathrm{SO_2}}\mathrm{SO_2}(t) + \alpha_{\mathrm{B}}\mathrm{B}(t) + \alpha_{\mathrm{O}}\mathrm{O}(t) + \beta \ln\left[1 + \frac{\mathrm{SO_2}(t)}{S_o} + \frac{\mathrm{B}(t)+\mathrm{O}(t)}{B_o + O_o}\right]. \qquad (4)$$

The first three terms on the right-hand side represent the direct effects of aerosol–radiation interactions, wherein sulfur dioxide and organic carbon are expected to have a cooling effect, whereas black carbon could have a warming effect (Penner et al. 1994; Chylek and Wong 1995).

The last term represents aerosol–cloud interactions, defined here as the first indirect, or Twomey, effect (Twomey 1977). This logarithmic term follows Charlson et al. (1992), yet is a highly simplified term given the complex processes underlying aerosol–cloud interactions (Boucher et al. 2013). Whereas the aerosol direct effect is proportional to atmospheric aerosol burden, assumed to follow linearly from SO_2, B, and O, the indirect effect of cloud brightening involves the ratios of SO_2 to the natural aerosol background, S_o, and the sum of B and O to their natural aerosol background, $B_o + O_o$, and is represented as becoming saturated (Twomey 1977; Wigley and Raper 1992; Boucher and Pham 2002). A further rationale for the functional form of Eq. (4) is provided in Stevens (2015, appendices A and B therein). For global-annual SO_2, B, and O emissions, we employ the most recent estimate from O'Rourke et al. (2021), although using estimates from Hoesly et al. (2018) or Smith et al. (2011) gives qualitatively similar results for the period of overlap.

Equation (4) permits for more detail than empirical studies that have rescaled IPCC AR4 or AR5 aerosol effective radiative forcing (e.g., Padilla et al. 2011; Aldrin et al. 2012; Schwartz 2018), yet still involves potentially consequential simplifications. For example, we neglect nonsulfate and noncarbonaceous precursor emissions, such as nitrate emissions, which could impact aerosol radiative forcing (e.g., Bellouin et al. 2011; Hauglustaine et al. 2014). Further, rapid tropospheric adjustments, such as the cloud lifetime effect, are potentially important (Albrecht 1989), though uncertain (Stevens and Feingold 2009; Gettelman 2015; Malavelle et al. 2017). Finally, aerosol forcing is found to be sensitive to emission location in some studies (Zhang et al. 2016; Gettelman and Sherwood 2016; Persad and Caldeira 2019) but insensitive in others (e.g., Fiedler et al. 2019).

To check whether Eq. (4) adequately represents historic variations in aerosol radiative forcing, we fit it to the effective aerosol radiative forcing from 10 CMIP6 models participating in the Radiative Forcing Model Intercomparison Project (RFMIP) and Aerosols and Chemistry Model Intercomparison Project (AerChemMIP) (Pincus et al. 2016). Figure 1 shows the least squares fit of Eq. (4) to these RFMIP and AerChemMIP simulations. After applying a 5-yr smoothing to the effective aerosol radiative forcing, the standard deviation across models is 0.43 W m^{-2} over 1850–2014. Over this interval, the root-mean-square residual between each model and the least squares fit of Eq. (4) has a mean value of 0.09 W m^{-2}, ranging from 0.07 to 0.14 W m^{-2}. If using solely SO_2, the root-mean-square residual is slightly larger, with a mean of 0.13 W m^{-2}, demonstrating that the inclusion of black and organic carbon improves the simple model fit. This small residual suggests that Eq. (4) affords sufficient flexibility to emulate the magnitude and temporal evolution of aerosol radiative forcing generated by more sophisticated models. That is, contributions to global-scale aerosol radiative forcing from nonsulfate and noncarbonaceous aerosols, rapid tropospheric adjustments, and spatial variability in aerosol emissions, as simulated in sophisticated models, can largely be absorbed by appropriate fitting of Eq. (4).

c. *Net radiative forcing*

To obtain net radiative forcing F_{net}, we sum time series of F_{aer} with nonaerosol effective radiative forcing from Smith et al. (2021), which overlap with observed temperatures from 1850 to 2019. These nonaerosol effective radiative forcing time series are updated AR5 time series that are extended to 2019 using the SSP2.45 scenario (Smith et al. 2021). Nonaerosol forcing agents include long-lived greenhouse gases, tropospheric and stratospheric ozone, land-use change, black carbon on snow, contrails, solar variability, and stratospheric water vapor. These terms together contribute a net positive forcing over the historical period. We address uncertainties in nonaerosol forcing by including a scaling parameter γ_p. We note that greater forcing uncertainty was estimated in AR5 for methane (e.g., Etminan et al. 2016; Hoesly et al. 2018) and solar forcing (e.g., Dudok de Wit et al. 2017). Persisting uncertainty in these nonaerosol forcing terms in the updated forcing data, insomuch as they allow for positive trends, is expected to shift the inferred lower bound on F_{aer} to more negative values (Stevens 2018).

Volcanic forcing is also taken from Smith et al. (2021), but it is important to account for the fact that the temperature response to volcanic forcing appears to be damped relative to the temperature response to other forcing. That is, volcanic forcing appears to have a forcing efficacy less than one (Meinshausen et al. 2011; Marvel et al. 2016; Ceppi and Gregory 2019). We admit for uncertainty in the efficacy of volcanic forcing by introducing a scaling parameter γ_v. Although our focus is on anthropogenic aerosol forcing, we account for uncertainties in volcanic aerosol forcing because of the possibility that it trades off against F_{aer}. In another approach, Stevens (2015) focused

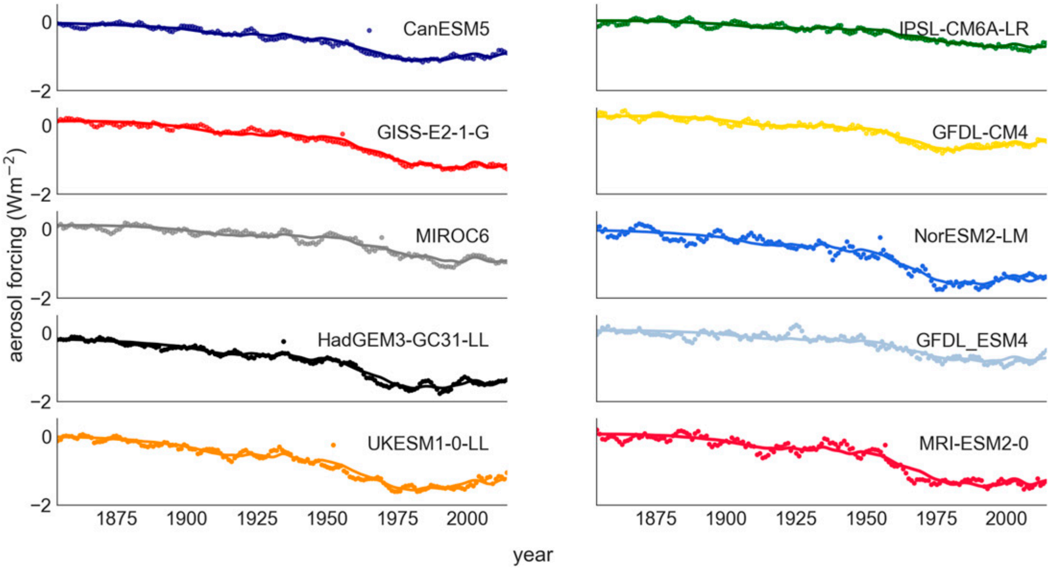

FIG. 1. Fits of Eq. (4) to time histories of aerosol forcing from 10 CMIP6 models participating in the Radiative Forcing Model Intercomparison Project (RFMIP) and Aerosols and Chemistry Model Intercomparison Project (AerChemMIP). Points are 5-yr smoothed values of aerosol forcing anomalies. For RFMIP simulations we calculate aerosol forcing anomalies as the difference of the piClim-Histaer and piClim-control experiments, and for AerChemMIP simulations we calculate anomalies using the histSST experiment relative to the histSST-piAer control experiment. The solid line is the least squares fit of Eq. (4) to each CMIP6 model simulation. Best fits suggest that the highly simplified aerosol model we use can approximate the evolution of historical effective aerosol radiative forcing from more sophisticated models. Furthermore, the parametric uncertainty represented in our Bayesian framework reflects model uncertainty associated with Eq. (4).

on the early record before 1950 as a period of relatively quiescent volcanism in order to separate F_{aer} from volcanic forcing. Such a time-limited approach is discussed in section 4a.

d. Bayesian priors and inversion

Our Bayesian model comprises 16 parameters: 6 associated with aerosol radiative forcing in Eq. (4), 3 associated with nonaerosol radiative forcing variance and the autocorrelation of internal variability, and 7 further temperature response parameters from Eq. (1). Note that the three temperature eigenmode weights α_n are constrained to sum to one, such that it is only necessary to invert for two eigenmode weights. We collectively refer to these 16 parameters as θ.

Table 1 summarizes the prior distribution specified for each parameter. Volcanic forcing efficacy γ_v is assigned a uniform prior from 0 to 1, consistent with findings of lower efficacy than for CO_2 (e.g., Meinshausen et al. 2011; Marvel et al. 2016; Gregory et al. 2016). For nonaerosol, nonvolcanic forcing efficacy γ_p, we assign a normal prior with mean of 1 and standard deviation 0.2. Equilibrium climate sensitivity $T_{2\times}$ is assigned a broad uniform prior from 1° to 10°C (Sherwood et al. 2020). The AR1 coefficient for internal variability, ρ, is specified as uniform from 0 to 1. Priors for τ_n and α_n are normal distributions with mean and standard deviation taken from Proistosescu and Huybers (2017). For adjusted forcing to a doubling of carbon dioxide $F_{2\times}$, we follow the Sherwood et al. (2020) normal prior with a mean of 4.0 W m^{-2} and standard deviation of 0.3 W m^{-2}.

There exist large and long-standing uncertainties associated with aerosol–radiation interactions (e.g., Bellouin et al. 2013; Su et al. 2013; Samset et al. 2014) and aerosol–cloud interactions (e.g., Carslaw et al. 2013; Gettelman 2015; Seinfeld et al. 2016; Feingold et al. 2016). The natural aerosol background parameters, S_o and $B_o + O_o$, are also uncertain (e.g., Carslaw et al. 2010; McCoy et al. 2015), despite their being fixed in previous analyses (e.g., Andronova and Schlesinger 2001; Aldrin et al. 2012; Skeie et al. 2014). Furthermore, to avoid circular reasoning (Rodhe et al. 2000; Anderson et al. 2003), the aerosol forcing prior should not be informed by temperature trends. Accordingly, we assume broad and uniform priors for the six aerosol parameters in Eq. (4) (see Table 1) that are only weakly informative in assuming a uniform distribution from −12 to 0 W m^{-2}. The prior constraint that F_{aer} is negative comes from process-based models (Bellouin et al. 2020). In comparison, Stevens (2015) bounded Eq. (4) such that present-day aerosol forcing varied between −1.5 and 0 W m^{-2}. Other analyses have also been found to be sensitive to the choice of prior (Frame et al. 2005; Hegerl et al. 2006; Annan 2015),

Following Bayes's rule, we invert for the joint posterior distribution of our 16 parameters θ,

$$P(\theta|T_{\mathrm{obs}}) \propto P(T_{\mathrm{obs}}|\theta)P(\theta), \tag{5}$$

where the likelihood $P(T_{\mathrm{obs}}|\theta)$ is formulated based on the multivariate Gaussian distribution of the difference between observed temperature and the forced response of our model:

TABLE 1. Model specification for the baseline inversion using temperature and forcing data from 1850 to 2019. Listed are posterior maximum likelihood estimates (MLE), the associated 5%–95% credible intervals (c.i.), and prior distributions for aerosol forcing parameters ($\alpha_{\mathrm{SO_2}}$,α_{B}, α_{O}, β, S_{o}, and $B_{\mathrm{o}} + O_{\mathrm{o}}$), volcanic efficacy ($\gamma_v$), nonaerosol forcing efficacy (γ_p), the AR1 coefficient of internal variability (ρ), and temperature response parameters (T_{2x}, τ_1, τ_2, τ_3, α_1, α_1, and F_{2x}). We also report the net aerosol forcing (F_{aer}), aerosol direct (F_{aer_d}), and aerosol indirect (F_{aer_i}) effects that are calculated from Eq. (4); the joint posterior distributions of aerosol parameters; and SO_2, B, and O time series, as described in section 2b. Aerosol forcing values are for the 2010–19 interval, with values for the 2000–10 interval given in parentheses. The parameter $\alpha_{\mathrm{SO_2}}$ has units of W m^{-2} (Tg SO_2 yr^{-1})$^{-1}$ and is multiplied by 10^3 in the table. Similarly, parameters α_{B} and α_{O} have units of W m^{-2} (Tg B yr^{-1})$^{-1}$ and W m^{-2} (Tg O yr^{-1})$^{-1}$, respectively, and are multiplied by 10^3. Columns μ and σ are the mean and standard deviation of normal prior distributions.

	Units	MLE	5% c.i.	95% c.i.	Prior distribution	Range	μ	σ
$\alpha_{\mathrm{SO_2}}$	See caption	−2.8	−5.5	−0.37	Uniform	−50 to 0	—	—
α_{B}	See caption	7	0.39	21	Uniform	−50 to 50	—	—
α_{O}	See caption	−16	−36	−8.5	Uniform	−50 to 50	—	—
β	W m^{-2}	−0.45	−0.80	−0.039	Uniform	−3 to 0	—	—
S_{o}	Tg SO_2	97	35	144	Uniform	10–200	—	—
$B_{\mathrm{o}} + O_{\mathrm{o}}$	Tg B + O	31	5.4	57	Uniform	10–60	—	—
ρ	—	0.70	0.59	0.77	Uniform	0–1	—	—
$T_{2\times}$	°C	3.4	1.8	6.1	Uniform	1–10	—	—
γ_v	—	0.72	0.59	0.97	Uniform	0–1	—	—
γ_p	—	1.01	0.75	1.3	Normal	—	1	0.2
τ_1	yr	0.67	0.30	1.1	Normal	—	0.7	0.25
τ_2	yr	12	4.9	21	Normal	—	9	7
τ_3	yr	352	221	482	Normal	—	354	80
α_1	—	0.20	0.069	0.38	Normal	—	0.24	0.15
α_2	—	0.38	0.12	0.57	Normal	—	0.32	0.15
$F_{2\times}$	W m^{-2}	4.0	3.5	4.5	Normal	—	4.0	0.3
F_{aer}	W m^{-2}	−0.85 (−0.95)	−1.3 (−1.4)	−0.50 (−0.56)	Uniform	−12 to 0	—	—
F_{aer_d}	W m^{-2}	−0.56	−0.91	−0.16	Uniform	−6 to 0	—	—
F_{aer_i}	W m^{-2}	−0.45	−0.99	−0.04	Uniform	−6 to 0	—	—

$$P(T_{\mathrm{obs}}|\theta) \sim N[T_{\mathrm{forced}}(\theta), \mathbf{\Sigma}^2(\theta)]. \qquad (6)$$

Sampling is performed using the Metropolis–Hastings algorithm (Metropolis et al. 1953; Hastings 1970), and we run three chains of one million samples. The first 5000 burn-in samples are discarded for each chain, and the remainder are thinned by a factor of 5 to reduce serial correlation. Results are consistent among chains, indicating that our model is adequately sampled. Reflecting how observed temperatures are represented, model temperatures between 1960 and 1990 are removed from each realization.

3. Results

Table 1 lists the maximum likelihood estimate (MLE) and 5%–95% posterior credible interval ranges for the 16 parameters, θ, as well as ranges for F_{aer} and aerosol direct and indirect effect forcing. Modeled and observed temperatures fit well, with the posterior 5%–95% posterior credible interval covering 99% of observations (Fig. 2). The credible interval is determined by integrating Eq. (1) using each posterior realization of θ and adding realizations of observational error and internal variability. A mismatch does appear, however, in the form of warmer-than-predicted temperatures observed in the early 1940s. This mismatch, noted in other attempts to reproduce surface temperature from forcing (Folland et al. 2018), likely arises because of systematic errors in the observations, given that such a warm anomaly is absent in nearshore land station temperature records (Cowtan et al. 2018) and is absent from sea surface temperature records after correcting for systematic biases associated with engine-room-intake and bucket estimates (Chan and Huybers 2021).

The posterior distribution of F_{aer} is calculated from the joint posterior distribution of aerosol parameters associated with Eq. (4) (Table 1). The posterior MLE for F_{aer} between 2000 and 2010, relative to 1750, is −0.95 W m^{-2}. The lower bound on F_{aer} is −1.4 W m^{-2} using a 5th percentile value or −1.5 W m^{-2} using a 1st percentile value. Calculating the lower bound over 2010–19, the posterior MLE for F_{aer}, again relative to 1750, is −0.85 W m^{-2}, and its lower bound is −1.3 W m^{-2} using a 5th percentile value (Fig. 2c), or −1.4 W m^{-2} using a 1st percentile value. The mean aerosol direct effect over 2010–19 is −0.56 W m^{-2} (from −0.91 to −0.16 W m^{-2} 5%–95% credible interval), and the mean aerosol indirect effect over 2010–19 is −0.45 W m^{-2} (from −0.99 to −0.04 W m^{-2} 5%–95% credible interval).

a. Origin of lower-bound constraints on anthropogenic aerosol forcing

Offsetting covariance among the six aerosol forcing parameters in Eq. (4) better constrains the overall range of F_{aer} than its individual components. The natural sulfate background, S_o, for instance, covaries with values of β with a Pearson correlation coefficient of $r = 0.32$. Thus, whereas a more negative value of F_{aer} can come about either through a greater indirect effect, β, or smaller natural aerosol background, the combination of these parameters is constrained.

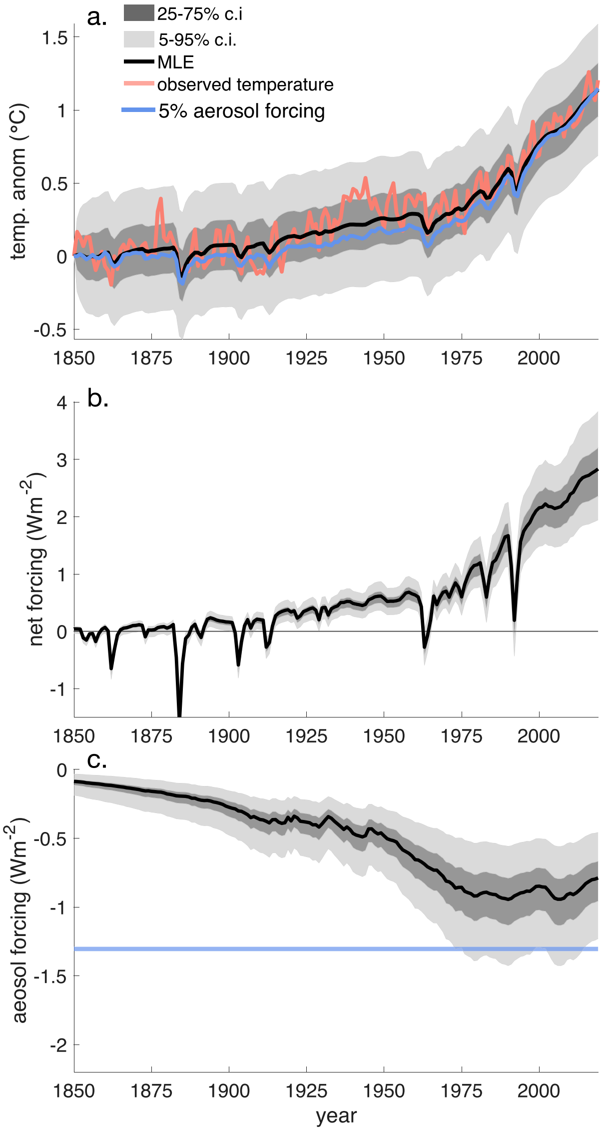

FIG. 2. Posterior estimates of temperature and forcing using data from 1850 to 2019. (a) Observed temperatures from HadCRUT4 (red) and the maximum likelihood estimates (MLE) of temperature (black), where each is referenced to an 1850 baseline. Also shown is temperature if aerosol radiative forcing is conditioned on its 5th percentile lower bound between 2010 and 2019 of $-1.3\ \mathrm{W\,m^{-2}}$ (light blue). (b) Net forcing comprising contributions from greenhouse gases, anthropogenic and volcanic aerosols, land-use change, tropospheric and stratospheric ozone, black carbon on snow, contrails, stratospheric water vapor, and solar variability. (c) Anthropogenic aerosol radiative forcing (F_{aer}) in terms of its MLE (black line) and its 5th percentile lower bound averaged over 2010–19 (blue line). Shading indicates 50% (dark gray) and 90% (light gray) credible intervals for annual averages.

The two direct effect coefficients for carbonaceous aerosols, α_{B} and α_{O}, are anticorrelated, with $r = -0.82$. Aerosol direct and indirect effects also trade off in capturing variability in observed temperature trends. Parameters $\alpha_{\mathrm{SO_2}}$ and β compensate, with $r = -0.54$, as do the aerosol direct and indirect effects, $r = -0.56$, in explaining observed temperature trends, such that the model cannot readily distinguish the aerosol direct from indirect effect. The parameter covariance, even in this highly simplified model, highlights the need for uncertainty quantification in higher-dimensional models, as discussed by Lee et al. (2016) and Carslaw et al. (2018).

We find general agreement between the MLE aerosol forcing parameters and the best-fit parameters across the 10 simulations in Fig. 1. The MLE β of $0.45\ \mathrm{W\,m^{-2}}$ is qualitatively similar to the best-fit β of $0.42\ \mathrm{W\,m^{-2}}$. Our MLE $\alpha_{\mathrm{SO_2}}$ of 2.8 is smaller than the best-fit value of $3.7\ \mathrm{W\,m^{-2}\,(Tg\,SO_2\,yr^{-1})^{-1}} \times 10^{-3}$, but our MLE S_o of 97 Tg SO_2 is also slightly smaller than the best-fit value across the simulations of 107 Tg SO_2, such that the overall effect is similar. The 10 simulations diverge on the sign and magnitude of the best-fit direct effect parameters for black and organic carbon, α_{B} and α_{O}, consistent with the notion that the direct effect parameters trade-off in capturing observed temperature trends. Note that the Bayesian framework better captures the covariance among these parameters than does the least squares fit used earlier for purposes of initial characterization.

Posterior constraints on the volcanic forcing efficacy parameter γ_v give a MLE value of 0.72 and a 5%–95% posterior credible interval of 0.59–0.97, indicating that the efficacy of volcanic forcing for producing a temperature response is less than that of carbon dioxide forcing. Previous estimates of volcanic efficacy range from 0.5 to 0.7 (e.g., Chylek et al. 2020; Marvel et al. 2016), consistent with our estimate, although these values were for AR5 volcanic forcing data. Performing our inversion with AR5 forcing data produces a MLE volcanic efficacy parameter of 0.67. Lehner et al. (2016), however, suggest that it is premature to infer that volcanic forcing has reduced efficacy because of the coincidence of volcanic eruptions and El Niño events over the twentieth century. A more detailed study of volcanism, El Niño events, and internal climate variability, possibly using this same framework, could be pursued in future work.

Perhaps surprisingly, γ_v does not substantially contribute to uncertainty in F_{aer}. The magnitude of F_{aer} and the volcanic forcing efficacy are weakly correlated ($r = -0.10$). This lack of correlation despite both terms being negative forcing reflects that volcanic forcing tends to decay more rapidly and shows little temporal covariance with trends in F_{aer}. Conditional on the 5% aerosol forcing lower bound, the MLE of γ_v is 0.71, with a similar posterior distribution to the posterior distribution that is not conditioned on 5% aerosol forcing. These results suggest that it is less essential to subselect time periods associated with low volcanic activity in order to isolate F_{aer}, at least when all terms are cointegrated within a Bayesian framework.

Unlike for volcanic forcing, we find that uncertainty in the efficacy of nonaerosol forcing γ_p, relative to values in Smith et al. (2021), is an important contribution to the uncertainty in F_{aer}. The MLE of γ_p is 1.01 with a 5%–95% posterior credible interval of 0.75–1.3. Conditional on the 5th percentile of F_{aer}, the MLE of γ_p is 1.3, giving the expected result that greater nonaerosol forcing allows for more negative values of F_{aer}. Conversely, if γ_p is assigned its MLE of 1.01, the 5th percentile of F_{aer} is $-1.1\ \mathrm{W\,m^{-2}}$.

For the first-order autoregressive coefficient, ρ, we find a MLE value of 0.70 with a 5%–95% credible interval of 0.59–0.77. The MLE value of ρ corresponds to an autocovariance time scale of $\tau = -1/\ln(\rho)$, or 2.5 years, with a 5%–95% credible interval of 1.9–3.8 years. Note that F_{aer} is only weakly sensitive to the time scale of internal variability, as represented using an AR1 process and drawn from the posterior distribution of ρ. If ρ is assigned its MLE value of 0.70, the 5th percentile of the F_{aer} distribution for 2010–19 is unchanged at $-1.3\,\mathrm{W\,m^{-2}}$. The narrow distribution of the autocovariance time scale τ may reflect that our representation does not capture low-frequency, interdecadal variability. In section 4c we discuss an extension that better accounts for internal variability at longer time scales.

b. *Relationship with climate sensitivity*

Our MLE climate sensitivity is 3.4°C and has a broad 5%–95% posterior credible interval of 1.8°–6.1°C. The higher mean and upper bound on ECS than in Sherwood et al. (2020) reflects contributions from the long-response time scale, which is almost unrealized in the historical record (Proistosescu and Huybers 2017). The loading on each eigenmode equals α_n times ECS and has an average that increases from 0.67 ($\tau_1 = 0.67\,\mathrm{yr}$) to 1.10 ($\tau_2 = 12\,\mathrm{yr}$) to 1.63°C ($\tau_3 = 352\,\mathrm{yr}$). The uncertainty on each eigenmode also increases with times scales: standard deviations for the loading on each eigenmode increase from 0.25° to 0.41° to 1.2°C.

Although not the focus of this study, it appears the difference in how informative the transient response is of the equilibrium response helps explain the wide range of foregoing upper bounds on climate sensitivity from empirical studies (e.g., Bodman and Jones 2016). Recent work suggests that as SST patterns evolve from their transient to their equilibrium state, they modulate the net radiative feedback, and, thus, the effective climate sensitivity (Andrews et al. 2015). Representing zonal equatorial temperature gradients appears especially important for capturing changes in radiative feedbacks (Dong et al. 2019). The resulting difference between the transient and long-term feedbacks is called a ‘‘pattern effect’’ and needs to be accounted for when inferring ECS from the fast response manifested over the historical record (e.g., Sherwood et al. 2020). Such a pattern effect is generally missing from previous simple models used in inversions of aerosol forcing and climate sensitivity, leading to a strong covariance between the transient and equilibrium feedbacks. In contrast, the pattern effect exhibits a large spread in general circulation models (Andrews et al. 2018) and cannot currently be constrained from the historical climate record (Sherwood et al. 2020).

The Proistosescu and Huybers (2017) model is a general approximation of the leading modes of response that allows for the presence of a pattern effect by allowing for different radiative feedbacks between the fast and slow modes. In this regard, our model appears more flexible than previous box models used for inferring F_{aer}. The three modes can be interpreted as representing time-evolving warming patterns associated with, for example, warming over land on annual time scales, the ocean mixed layer on decadal time scales, and the eventual warming of the deep ocean on centennial time scales. Each mode is assumed to have a different underlying surface temperature pattern and, thus, a different radiative feedback. As the relative loading of each mode changes, so does the SST pattern and the net radiative feedback. The lack of constraints on the long-term feedback and, thus, on the ECS can be understood as a consequence of the fact that this long time scale is almost entirely unrealized in observations.

Previous inverse (e.g., Forest 2018) or coupled model studies (e.g., Andreae et al. 2005; Chylek et al. 2016) found a strong relationship between F_{aer} and climate sensitivity, whereas Smith et al. (2020) do not find such a relationship in the CMIP6 ensemble. We obtain a correlation between the *net* forcing and the fast-mode response, here defined as the summed response of the annual and decadal modes, of $r = -0.76$, or between the net forcing and climate sensitivity of $r = -0.52$. The correlation between F_{aer} and ECS, however, is only $r = 0.01$ on account of uncertainty in the relationship between the fast-mode response and ECS as well as between F_{aer} and F_{net}. That said, this low correlation does not fully capture dependencies between F_{aer} and ECS. Conditioned on the 5th percentile value of the climate sensitivity distribution, the 2010–19 F_{aer} 5th percentile value is $-1.1\,\mathrm{W\,m^{-2}}$, whereas when conditioned on 95th percentile climate sensitivity the 5th percentile of F_{aer} becomes $-1.3\,\mathrm{W\,m^{-2}}$. Figure 3 illustrates how, despite the lack of a linear relationship, the magnitude of F_{aer} sets the range of other parameters, including the net forcing and the temperature response across different time scales.

4. Discussion

The Bayesian framework allows us to explore how the observational record constrains F_{aer} and climate sensitivity through quantifying how different processes combine to allow fitting to the data within uncertainties, similar to the ‘‘storyline’’ approach outlined for constraining climate sensitivity in Stevens et al. (2016). We are particularly interested in reconciling our lower bound with more negative estimates (Bellouin et al. 2020) and, thus, examine several modifications that would alter our 2010–19 5th percentile F_{aer} estimate of $-1.3\,\mathrm{W\,m^{-2}}$ to values around $-2.0\,\mathrm{W\,m^{-2}}$.

a. *Constraining aerosol forcing using pre-1950 data versus the full record*

Stevens (2015) used a shorter interval less influenced by volcanic activity and obtained a 2005 F_{aer} lower bound of $-1.3\,\mathrm{W\,m^{-2}}$ when employing global energy balance arguments. If only fitting our model using temperature and forcing from 1850 to 1950, we instead obtain a MLE F_{aer} of $-1.4\,\mathrm{W\,m^{-2}}$ and a 5th percentile lower bound of $-2.0\,\mathrm{W\,m^{-2}}$ for the 2000–10 interval. For 2010–19, we obtain a MLE F_{aer} of $-1.3\,\mathrm{W\,m^{-2}}$ and a 5th percentile lower bound of $-1.8\,\mathrm{W\,m^{-2}}$.

We illustrate the origin of the more negative bound on F_{aer} than in Stevens (2015) when only fitting to data before 1950 by sequentially modifying three parameters within our model. First, we used broad priors on the aerosol direct effect parameters, $\alpha_{\mathrm{SO_2}}$, α_{B}, and α_{O}, thus allowing for a more linear relationship between F_{aer} and precursor emissions, which addresses the particular critique of Stevens (2015) by Kretzschmar et al. (2017)

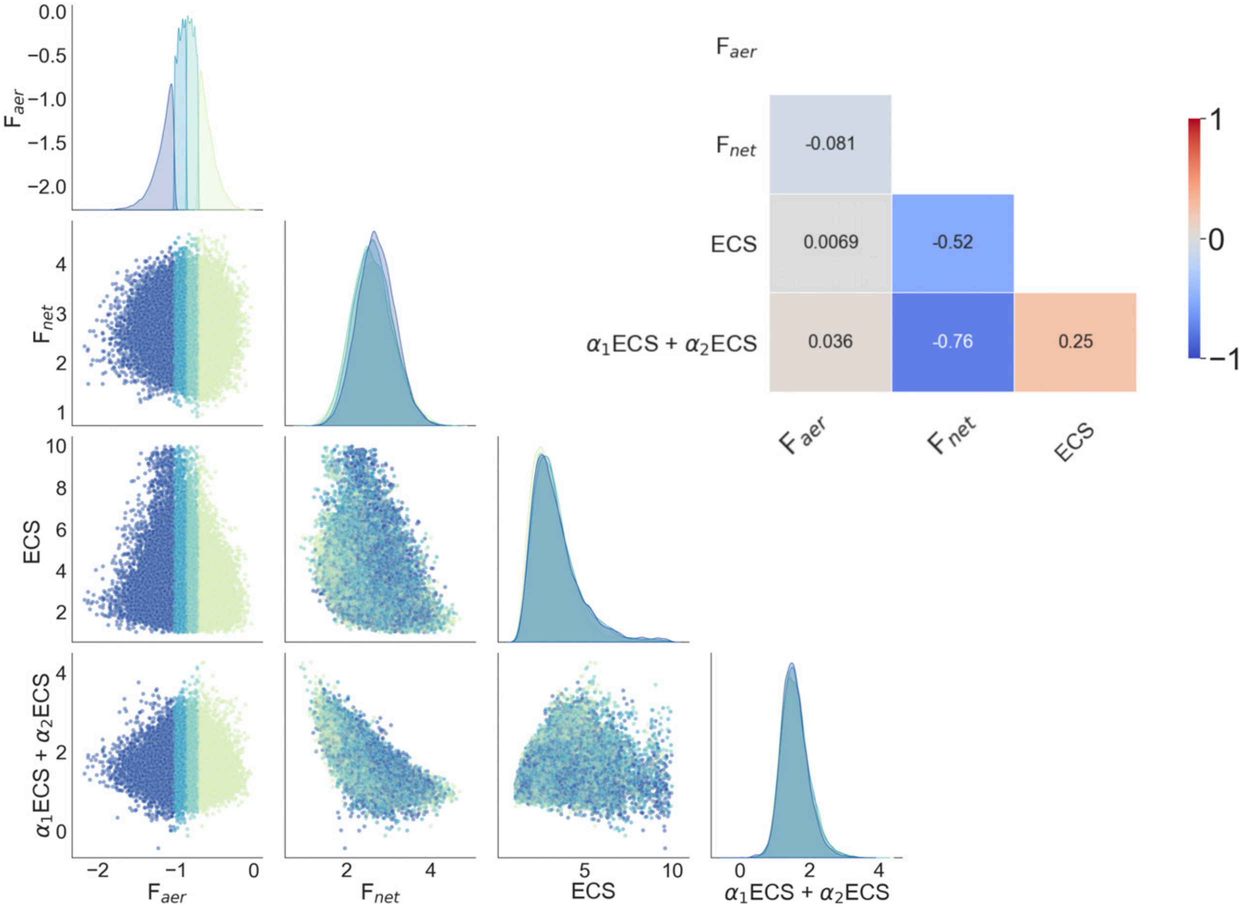

FIG. 3. Parameter covariance among aerosol forcing ($F_{\rm aer}$), net radiative forcing ($F_{\rm net}$), climate sensitivity (ECS), and the fast-mode temperature response to forcing (annual contributions from $\alpha_1 \times$ ECS plus decadal from $\alpha_2 \times$ ECS). Binning aerosol forcing by quartiles, shown from the lower quartile (blue) to upper quartile (yellow), illustrates how aerosol forcing influences the permissible range of other terms. The inset shows Pearson correlation coefficients between pairs of terms.

and Booth et al. (2018) that aerosol forcing could be more linear than logarithmic with emissions. If $\alpha_{\rm SO_2}$, $\alpha_{\rm B}$, and $\alpha_{\rm O}$ are fixed at their MLE values, the 5th percentile lower bound on 2000–10 $F_{\rm aer}$ becomes $-1.7\,{\rm W\,m^{-2}}$. Second, we incorporated non-aerosol forcing terms beyond solely long-lived greenhouse gas forcing. Excluding all but these greenhouse gas forcing terms gives a 5th percentile of $F_{\rm aer}$ equal to $-1.6\,{\rm W\,m^{-2}}$. Finally, we allowed for uncertainty in temperature observations and internal variability that, if excluded, yields a 5th percentile bound of $-1.6\,{\rm W\,m^{-2}}$. Considering these modifications jointly, we can obtain values commensurate with Stevens (2015). Fixing aerosol direct effect parameters at their MLE values, excluding all radiative forcing except that from long-lived greenhouse gases, and excluding uncertainty in temperature observations and internal variability yields a 2000–10 5th percentile aerosol forcing lower bound of $-1.2\,{\rm W\,m^{-2}}$. This bound is slightly tighter than the Stevens (2015) bound, possibly on account of employing temperature trends rather than comparing net forcing in 1850 and 1950.

Our approach addresses several critiques of the Stevens (2015) framework (Kretzschmar et al. 2017; Booth et al. 2018; Stevens 2018) and indicates that the approach taken by Stevens (2015) gives a larger-magnitude lower bound on aerosol forcing when accounting for additional uncertainties. The fact that our baseline estimate of aerosol radiative forcing is similar to Stevens (2015) is a coincidence whereby greater uncertainties are offset by additional constraints available from considering a longer time series and additional structure in the aerosol emissions and temperature histories.

b. The role of temporal structure in separating forcing from sensitivity

It has been suggested that a primary source of uncertainty in constraining aerosol forcing is compensation between radiative forcing and climate sensitivity in explaining historical temperature trends (Andreae et al. 2005; Kiehl 2007; Knutti et al. 2017). This compensation appears when restricting the analysis prior to the 1950s, but less so afterward. Whereas the anticorrelation between ECS and $F_{\rm aer}$ is weak using data from 1850 to 2019 ($r = -0.01$), after restricting to 1850–1950 the anticorrelation increases to -0.30. Using only pre-1950 data, we obtain a highly uncertain ECS distribution with a 5%–95% credible interval of 2.3°–9.1°C and a MLE value of 5.2°C.

In our framework, limiting model fitting to temperatures from 1850 to 1950 results in a posterior temperature distribution with too much cooling between 1950 and 1980, followed by too much warming (Figs. 4a,b). That is, increased aerosol precursor emissions between 1950 and 1980 cause excessive cooling, and a plateau in emissions after 1980 unmasks the high climate sensitivity and produces excessive warming relative to observations. We infer that the temporal evolution of aerosol precursor emissions and temperature post-1950 results in a reduced capacity for aerosol forcing and sensitivity to trade off against each other in explaining temperature trends.

Previous studies have also pointed to the important role of differences in the post-1950 evolution of aerosol forcing and temperature trends. In the GFDL Global Atmosphere and Land Model AM4.0/LM4.0 (Zhao et al. 2018) and DOE E3SM Coupled Model version 1 (Golaz et al. 2019), strongly negative F_{aer} and high climate sensitivity led to mismatches between modeled and observed temperatures. In particular, these models simulated reduced warming in the 1960s–1980s, followed by an excessive warming trend after aerosol emissions peak around 1980. When using the Held et al. (2010) two-layer energy balance model to emulate their coupled model temperature response, Golaz et al. (2019) found it necessary to reduce F_{aer} from $-1.65\ \mathrm{W\,m^{-2}}$ to approximately $-0.8\ \mathrm{W\,m^{-2}}$ and ECS from 5.3° to 2.7°C in order to improve the fit of modeled to observed temperatures, qualitatively in keeping with our findings.

c. Increased internal or observational variability

The treatment of low-frequency internal variability was highlighted by Forest (2018) as a key open issue for constraining F_{aer}. Indeed, an important difference in foregoing inverse model studies that obtained a lower bound around $-2.0\ \mathrm{W\,m^{-2}}$ appears to be the fact that they allow for more low-frequency internal variability or observational error (e.g., Aldrin et al. 2012; Skeie et al. 2014, 2018). We examine how the lower bound of F_{aer} depends on the specification of the variance of internal variability σ^2_{int} and its autocorrelation ρ. An increase in ρ is motivated by the appearance of greater decadal autocorrelation than would be expected if temperature variations followed an AR1 process (e.g., Vyushin and Kushner 2009; Laepple and Huybers 2014), and that observational products show temperature trends that lie outside the range of temperature variability simulated by coupled models in historical runs (e.g., Zhou et al. 2016; Coats and Karnauskas 2017; Hegerl et al. 2018; Parsons et al. 2020).

One means to obtain an estimate of the autocorrelation of low-frequency internal variability is to calculate the AR1 coefficient ρ from global-mean, detrended temperature time series from 39 CMIP6 coupled model control runs using 10-yr block-averaged temperatures. From block-averaged temperatures, we obtain a mean AR1 coefficient of 0.33 across the 39 simulations. This value implies a mean annual AR1 coefficient of 0.90, where $\rho_{\mathrm{annual}} = (\rho_{\mathrm{block}})^{1/n}$ and n is the number of years in the block. We obtain a 5th percentile of F_{aer} equal to $-1.7\ \mathrm{W\,m^{-2}}$ (MLE $-1.1\ \mathrm{W\,m^{-2}}$) for 2000–10, or $-1.6\ \mathrm{W\,m^{-2}}$ (MLE $-1.0\ \mathrm{W\,m^{-2}}$) for 2010–19 after increasing ρ from 0.5 to 0.90 and doubling innovation variance σ^2_{int} from its CMIP6 ensemble mean value of 0.019° to 0.036°C^2 (Figs. 4c,d). Increasing innovation variance to 0.037°C^2 is within the range simulated by 39 CMIP6 control simulations, which have a maximum value of 0.060°C^2. These modifications increase the variance of the AR1 process fivefold, where variance is $\sigma^2_{\mathrm{int}}/(1-\rho^2_{\mathrm{annual}})$.

Similar to increased internal variability, representing greater error in observations also permits for a more negative lower bound on F_{aer} (Figs. 4e,f). In particular, low-frequency observational errors in sea surface temperatures could occur at the multidecadal time scales of instrumentation changes (Chan et al. 2019). We add AR1 observational error, similar to the term for internal variability in Eq. (3), with observational error variance estimated as the offset between modeled and observed temperatures between 1936 and 1948, which has a mean of 0.14°C, or 0.02°C^2 (e.g., Fig. 2a). If we assume this variance of 0.02°C^2 and an AR1 coefficient of 0.9, independent of increasing internal variability, we obtain a 5% F_{aer} lower bound of $-1.6\ \mathrm{W\,m^{-2}}$ for 2000–10, or $-1.5\ \mathrm{W\,m^{-2}}$ for 2010–19. Estimating bounds using both increased internal variability and observational error leads to a MLE of $-1.2\ \mathrm{W\,m^{-2}}$ and 5% lower bound on F_{aer} of $-1.9\ \mathrm{W\,m^{-2}}$ for 2000–10, or $-1.8\ \mathrm{W\,m^{-2}}$ for 2010–19 (Figs. 4e,f).

d. Ocean heat content

Ocean heat content observations could, conceivably, further constrain F_{aer}. The covariance between F_{aer} and ocean heat uptake noted in previous work (e.g., Forest et al. 2002; Forest 2018) argues for inferring both jointly. Skeie et al. (2014) and Johansson et al. (2015) state the importance of ocean heat content observations, yet other studies find that incorporating these observations only weakly constrains climate sensitivity (Knutti et al. 2002; Aldrin et al. 2012) and is influenced by the data source, depth covered, and observational uncertainties (Sokolov et al. 2010).

To explore whether additional constraints on F_{aer} can be obtained from ocean heat content observations, we compare the top-of-atmosphere radiative imbalance predicted by our climate response model with the radiative imbalance estimated from observed ocean heat content estimates. The Proistosescu and Huybers (2017) model that we build upon predicts the global net top-of-atmosphere radiative imbalance $N_{\mathrm{forced}}(t)$ as the difference between net forcing F_{net} and the radiative response to forcing,

$$N_{\mathrm{forced}}(t) = F_{\mathrm{net}}(t) - \sum_{n=1}^{3} \lambda_n T_n(t), \qquad (7)$$

where $T_n(t)$ is given by Eq. (1), and λ_n is the radiative feedback associated with each mode of the response. Values of $T_n(t)$ are drawn from our posterior distribution, and values of λ_n are the median radiative feedback coefficients from Proistosescu and Huybers (2017) that were obtained by fitting to CMIP5 simulations.

We compare our results to the top-of-atmosphere radiative imbalance implied by the full-depth ocean heat uptake

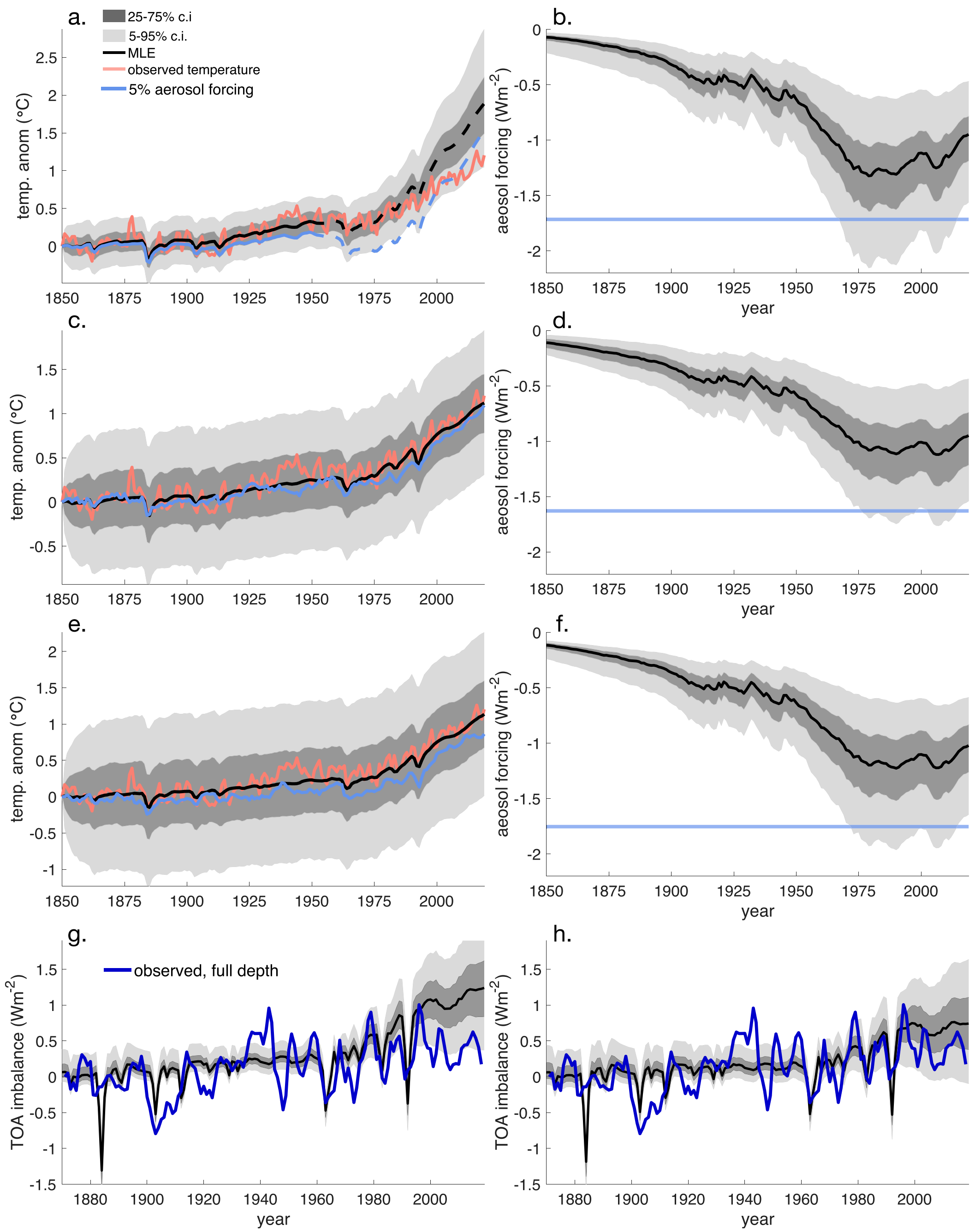

FIG. 4. Posterior estimates of temperature and forcing from various scenarios. (a),(b) Only using data from 1850 to 1950 results in a MLE (solid black line) that predicts warmer temperatures after the 1990s (dashed black line) than observed (red line). Constraining the model to the 5th percentile of aerosol radiative forcing (solid blue line) leads to excessive cooling between 1950 and 1990, followed by stronger warming than observed (dashed blue line). Aerosol radiative forcing is both more negative and more uncertain relative to using the full period (Fig. 2). (c),(d) Increasing the variance of internal variability by a factor of 5, and (e),(f) additionally including similar low-frequency observational error, leads to larger credible intervals. Posterior credible intervals are shown at 50% (dark gray) and 90% (light gray) coverage. Observed and simulated temperatures are referenced to an 1850 baseline. (g) Modeled top-of-atmosphere radiative imbalances (black line) using the median values of CMIP5-inferred radiative damping parameters [λ_n in Eq. (7)]. Radiative imbalances are estimated from ocean heat content estimates Zanna et al. (2019) divided by 0.9. (h) As in (g), but after increasing radiative damping [i.e., λ_n in Eq. (7)].

estimates of Zanna et al. (2019), after dividing ocean heat uptake rates by 0.9, under the assumption that 90% of Earth's energy imbalance is absorbed by the ocean (von Schuckmann et al. 2020). Uncertainties remain, however, regarding how heat uptake is partitioned among the upper and lower ocean, atmosphere, cryosphere, and land system (e.g., Hansen et al. 2005; Cheng et al. 2017).

Comparison of our maximum likelihood estimate of the top-of-atmosphere radiative imbalance against the implied estimate from Zanna et al. (2019) indicates a mismatch in the 1940s and after 1980 (Fig. 4g). Given that the ocean heat uptake estimated by Zanna et al. (2019) is based upon propagating SSTs into the ocean interior, the mismatch in the 1940s may be the result of SST errors during this time period (Cowtan et al. 2018; Chan and Huybers 2021). The fact that our model produces a larger top-of-atmosphere radiative imbalance than estimated by Zanna et al. (2019) after 1980, however, suggests that the recent rate of planetary heat uptake is poorly fit with climate response parameters estimated from the CMIP5 simulations.

For the median CMIP5 λ_n parameters, the MLE of the radiative imbalance from 2006 to 2019, referenced to an 1870 baseline, is 1.16 $\mathrm{W\,m^{-2}}$ (0.45–1.94, 5%–95% credible interval). Sherwood et al. (2020), however, report a MLE of the radiative imbalance of 0.80 $\mathrm{W\,m^{-2}}$ (0.55–1.04, 5%–95% credible interval) for 2006–18. Discrepancies in λ_n are also found in recent work suggesting that coupled GCMs exhibit too little radiative damping relative to GCMs forced with observed SSTs (Zhou et al. 2016; Sherwood et al. 2020). The radiative response to forcing is defined by the second term in Eq. (7), $R = \sum_{n=1}^{3}\lambda_n T_n(t)$, and a too small R leads to an overestimate of the top-of-atmosphere radiative imbalance.

As a heuristic example, we increase λ_n from their CMIP5-fit values of $\lambda_1 = 1.6, \lambda_2 = 1.4$, and $\lambda_3 = 0.8\,\mathrm{W\,m^{-2}\,°C^{-1}}$ to $\lambda_1 = 2.2$, $\lambda_2 = 1.8$, and $\lambda_3 = 0.8\,\mathrm{W\,m^{-2}\,°C^{-1}}$, increasing the net feedback over the historical period from -1.45 to $-1.95\,\mathrm{W\,m^{-2}\,K^{-1}}$, consistent with a $\Delta\lambda = 0.5\,\mathrm{W\,m^{-2}\,K^{-1}}$ mean bias between coupled simulations and simulations prescribed with observed SST patterns (Sherwood et al. 2020). Increased radiative damping decreases the predicted top-of-atmosphere radiative imbalance and increases consistency with ocean heat uptake estimates (Fig. 4h), with MLE radiative imbalance becoming 0.71 $\mathrm{W\,m^{-2}}$ (from -0.02 to 1.54 5%–95% credible interval).

We are thus concerned that biases in simulated radiative damping and planetary heat uptake over recent decades implies that emulators trained on coupled models are similarly biased. Specifically, the discrepancy between the observed planetary heat uptake and net top-of-atmosphere radiative imbalance from coupled models can be thought of as a "ghost forcing." Experiments with prescribed SSTs suggest that this ghost forcing is due to historical SSTs causing a stronger radiative damping and more negative cloud feedback than SSTs in coupled models (Zhou et al. 2016). An inversion with priors informed by coupled models, however, can erroneously attribute this ghost forcing to more negative radiative forcing F_{net}. We speculate that the weakened radiative damping in coupled models leads to inferences of F_{aer} that are biased low when attempting to fit to recent planetary heat uptake. Indeed, a recent paper by Smith et al. (2021) using emulators trained on coupled models finds that the MLE value of F_{aer} becomes more negative by 0.2 $\mathrm{W\,m^{-2}}$ when also fitting planetary heat uptake. In our formulation, the uncertainties in radiative damping are encapsulated in uncertainties in λ_n. Given the lack of independent observational constrains on the true radiative damping and uncertainty about whether recent SST patterns that cause more negative feedbacks are forced or unforced (Andrews et al. 2018; Sherwood et al. 2020), we conclude that ocean heat content data at present do not offer robust additional constraints on F_{aer}. We also note that trends in ocean heat content prior to the 1950s have potentially important uncertainties, particularly in the deep ocean (Gebbie and Huybers 2019).

e. *Reconciling our estimates with foregoing aerosol forcing lower bounds*

Our alternate 2000–10 5% aerosol forcing lower bound of $-1.7\,\mathrm{W\,m^{-2}}$ when including a factor of 5 increase in internal variability is similar to previous finding of a 5% lower bound of $-1.7\,\mathrm{W\,m^{-2}}$ by Aldrin et al. (2012) and Skeie et al. (2014), or a $-1.8\,\mathrm{W\,m^{-2}}$ lower bound by Skeie et al. (2018). These studies reference their lower bounds to a baseline around 2010, such that our 2000–10 is comparable. These foregoing studies used a different model setup than our analysis—for example, including hemispheric temperatures—making it difficult to directly compare the magnitudes of observational error allowed for in foregoing studies, but their specified uncertainties were substantial. Aldrin et al. (2012) specifies AR1 coefficients ranging from 0.5 to 0.9 and hemispheric standard deviations of 0.5°–0.6°C, as well as AR1 model error and a representation of internal variability based on the Southern Oscillation. The posterior distribution of F_{aer} obtained by Aldrin et al. (2012) is nearly identical to their F_{aer} prior distribution from AR5, implying that their observations provide little further constraint on F_{aer}. Skeie et al. (2014, 2018) use a similar approach but also include an autoregressive order three process, i.e., AR3, representing long-term internal variability estimated from long, coupled model control simulations.

A recent study by Smith et al. (2021) uses a similar framework to ours and obtained a 2019 maximum likelihood estimate of $-0.9\,\mathrm{W\,m^{-2}}$ and 5% aerosol forcing lower bound, referenced to 1750, of $-1.6\,\mathrm{W\,m^{-2}}$ (their Table S4), compared to our MLE of $-0.85\,\mathrm{W\,m^{-2}}$ and 5% lower bound of $-1.3\,\mathrm{W\,m^{-2}}$. They use the same aerosol forcing model as in Eq. (4) and a simple emulator for the temperature response to forcing. We hypothesize that three methodological differences account for the approximately 0.3 $\mathrm{W\,m^{-2}}$ discrepancy in the 5% lower bounds in their and our estimate: the use of ocean heat uptake observations, the treatment of observational error, and the treatment of internal climate variability. First, regarding ocean heat uptake, Smith et al. (2021) provide an estimate of aerosol forcing lower bound solely based on observed temperatures, with a MLE of $-0.80\,\mathrm{W\,m^{-2}}$ and a less negative lower bound of 2019 aerosol forcing of $-1.4\,\mathrm{W\,m^{-2}}$. Second, we use time-resolved observational error from HadCRUT4, whereas Smith et al. (2021) use a time-mean value of $0.01°\mathrm{C}^2$. Repeating our inversion with a fixed observational error of $0.01°\mathrm{C}^2$ lowers the 2019 5% lower bound by 0.1 $\mathrm{W\,m^{-2}}$ to $-1.4\,\mathrm{W\,m^{-2}}$. These two factors already bring our lower bound in line with the Smith et al. (2021) lower bound. Differing treatment of internal variability can further explain differences in the lower bounds. Smith et al. (2021) draw realizations of internal variability from detrended CMIP6 preindustrial control global mean temperature anomalies. We first fix internal variability at the CMIP6 ensemble mean value and in section 4c show that increasing variability by a factor of 5 relative to this CMIP6 mean yields a 2019 5% lower bound of $-1.6\,\mathrm{W\,m^{-2}}$, more negative than the Smith et al. (2020) lower bound when they exclude constraints based on ocean heat uptake.

5. Conclusions

We find that an extension of the Stevens (2015) aerosol forcing model [Eq. (4)], also recently used by Smith et al. (2021), emulates global-annual historical variations in aerosol radiative forcing simulated by 10 state-of-the-art general circulation models. Simulations include contributions from rapid tropospheric adjustments, such as the cloud lifetime effect, and spatial variability in aerosol emissions. The root-mean-square residual between each simulation of global aerosol radiative forcing and a least squares fit using Eq. (4) has a mean value of $0.09\,\mathrm{W\,m^{-2}}$ when the global-annual sulfur dioxide, black carbon, and organic carbon aerosol precursor emissions used in each simulation are prescribed. Furthermore, using a simple aerosol forcing model that emulates the time history of aerosol forcing in CMIP6 models together with parametric uncertainty estimated using a Bayesian framework affords greater flexibility than previous approaches that rely upon rescaling aerosol forcing from GCM simulations (e.g., Padilla et al. 2011; Aldrin et al. 2012; Schwartz 2018).

Our analysis supports a lower bound on F_{aer} that is closer to -1.0 than to $-2.0\,\mathrm{W\,m^{-2}}$. Specifically, we obtain a 95% credible interval on F_{aer} between 2010 and 2019 from -1.3 to $-0.50\,\mathrm{W\,m^{-2}}$, despite ECS being broadly uncertain with a 95% credible interval from 1.8° to 6.1°C. Paleoclimate and process-based constraints elsewhere were argued to yield a tighter upper bound on climate sensitivity than do inferences from the historical record alone (e.g., Sherwood et al. 2020). To ensure that we accurately represent uncertainties in F_{aer}, it is important to jointly infer climate sensitivity and F_{aer}. In practice, however, we find that there is little correlation between climate sensitivity and F_{aer}, apparently because of distinct temporal variability. Similarly, uncertainty in effective volcanic forcing contributes little uncertainty to F_{aer} because their time histories weakly covary.

The origin of the strong F_{aer} constraint is traced to the rapid increase in precursor emissions between 1950 and 1980 and relatively stable emissions thereafter. Support for this emissions structure being critical comes from a restricted analysis using pre-1950 data that yields a 5th percentile 2010–19 lower bound on F_{aer} of $-1.8\,\mathrm{W\,m^{-2}}$ (Figs. 4a,b). In order for our model results to admit a 2010–19 fifth-percentile lower bound of $-1.6\,\mathrm{W\,m^{-2}}$, when employing the historical temperature record from 1850 to 2019, requires increasing the variance of internal variability by a factor of 5 relative to the mean variance inferred from 39 CMIP6 control simulations (Figs. 4c,d). Allowing for comparable variance in global-annual temperature observations further reduces this 2010–19 lower bound to $-1.8\,\mathrm{W\,m^{-2}}$ (Figs. 4e,f). It seems premature to rule out such large values of temperature variance, given differences between coupled and historical atmosphere-only model runs (e.g., Zhou et al. 2016; Parsons et al. 2020), differences between climate model and paleoclimate proxies (Laepple and Huybers 2014), and recent work on systematic SST errors (e.g., Chan and Huybers 2019).

There are several avenues open for improving empirical constraints on F_{aer}. One approach is to test our inference methodology within the context of general circulation model simulations. Temperatures simulated in response to various aerosol emissions and nonaerosol radiative forcing scenarios could be incorporated into our Bayesian methodology to infer F_{aer} and results compared against simulated values. Better quantifying uncertainty associated with low-frequency natural variability and observational error, presently not well characterized in GCMs and SST datasets, would also improve our ability to rule out extreme values of F_{aer}. Ocean heat uptake data cannot, at present, be used as an independent constraint on F_{aer} because radiative damping and net radiative forcing compensate in explaining observed variability in the historical top-of-atmosphere radiative imbalance. Improving the characterization of radiative feedback terms would allow for stronger constraints on F_{aer} from ocean heat uptake data. Further development of a Bayesian methodology to improve estimates of radiative feedbacks, low-frequency internal variability, and observational error should help narrow the stubborn bounds on aerosol radiative forcing.

Acknowledgments. HadCRUT4 historical global-mean surface temperatures from Cowtan and Way (2014), version 2.0, are available at https://www-users.york.ac.uk/~kdc3/papers/coverage2013/series.html. Transient effective aerosol forcing data from the RFMIP and AerChemMIP experiments in CMIP6 were accessed at https://esgf-node.llnl.gov/search/cmip6/. Sulfur dioxide, black carbon, and organic carbon data are from O'Rourke et al. (2021), accessed at https://doi.org/10.5194/gmd-11-369-2018-supplement. Temperature time series from the 40-member Community Earth System Model version 1 Large Ensemble (CESM1 LE) are from Kay et al. (2015), and global-mean temperature time series from CMIP5 control runs were downloaded from https://esgf-node.llnl.gov/projects/cmip5/. We thank Chris Smith for providing updated effective nonaerosol radiative forcing data, Karen McKinnon for assistance in obtaining the CESM1 LE data, Ted Amdur for processing global-mean temperature time series from CMIP5 control runs, and Luke Parsons for processing global-mean temperature time series from CMIP6 control runs. This work was supported by the Harvard University Climate Change Solutions Fund. C.P. acknowledges support from NOAA Grant UWSC12184 and a JISAO postdoctoral fellowship from the University of Washington.

REFERENCES

Albrecht, B. A., 1989: Aerosols, cloud microphysics, and fractional cloudiness. *Science*, **245**, 1227–1230, https://doi.org/10.1126/science.245.4923.1227.

Aldrin, M., M. Holden, P. Guttorp, R. Skeie, G. Myhre, and T. K. Berntsen, 2012: Bayesian estimation of climate sensitivity based on a simple climate model fitted to observations of hemispheric temperatures and global ocean heat content. *Environmetrics*, **23**, 253–271, https://doi.org/10.1002/env.2140.

Anderson, T. L., R. J. Charlson, S. E. Schwartz, R. Knutti, O. Boucher, H. Rodhe, and J. Heintzenberg, 2003: Climate forcing by aerosols—A hazy picture. *Science*, **300**, 1103–1104, https://doi.org/10.1126/science.1084777.

Andreae, M. O., C. D. Jones, and P. M. Cox, 2005: Strong present-day aerosol cooling implies a hot future. *Nature*, **435**, 1187–1190, https://doi.org/10.1038/nature03671.

Andrews, T., J. M. Gregory, and M. J. Webb, 2015: The dependence of radiative forcing and feedback on evolving patterns of surface temperature change in climate models. *J. Climate*, **28**, 1630–1648, https://doi.org/10.1175/JCLI-D-14-00545.1.

——, and Coauthors, 2018: Accounting for changing temperature patterns increases historical estimates of climate sensitivity. *Geophys. Res. Lett.*, **45**, 8490–8499, https://doi.org/10.1029/2018GL078887.

Andronova, N., and M. Schlesinger, 2001: Objective estimation of the probability density function for climate sensitivity. *J. Geophys. Res.*, **106**, 22 605–22 611, https://doi.org/10.1029/2000JD000259.

Annan, J., 2015: Recent developments in Bayesian estimation of climate sensitivity. *Curr. Climate Change Rep.*, **1**, 263–267, https://doi.org/10.1007/s40641-015-0023-5.

Bellouin, N., J. Rae, A. Jones, C. Johnson, J. Haywood, and O. Boucher, 2011: Aerosol forcing in the Climate Model Intercomparison Project (CMIP5) simulations by HadGEM2-ES and the role of ammonium nitrate. *J. Geophys. Res.*, **116**, D20206, https://doi.org/10.1029/2011JD016074.

——, G. W. Mann, M. T. Woodhouse, C. Johnson, K. S. Carslaw, and M. Dalvi, 2013: Impact of the modal aerosol scheme GLOMAP-mode on aerosol forcing in the Hadley Centre global environmental model. *Atmos. Chem. Phys.*, **13**, 3027–3044, https://doi.org/10.5194/acp-13-3027-2013.

——, and Coauthors, 2020: Bounding global aerosol radiative forcing of climate change. *Rev. Geophys.*, **58**, e2019RG000660, https://doi.org/10.1029/2019RG000660.

Bodman, R. W., and R. N. Jones, 2016: Bayesian estimation of climate sensitivity using observationally constrained simple climate models. *Wiley Interdiscip. Rev.: Climate Change*, **7**, 461–473, https://doi.org/10.1002/wcc.397.

Booth, B. B., G. R. Harris, A. Jones, L. Wilcox, M. Hawcroft, and K. S. Carslaw, 2018: Comments on "Rethinking the lower bound on aerosol radiative forcing." *J. Climate*, **31**, 9407–9412, https://doi.org/10.1175/JCLI-D-17-0369.1.

Boucher, O., and M. Pham, 2002: History of sulfate aerosol radiative forcings. *Geophys. Res. Lett.*, **29**, 221–224, https://doi.org/10.1029/2001GL014048.

——, and Coauthors, 2013: Clouds and aerosols. *Climate Change 2013: The Physical Science Basis*, T. F. Stocker et al., Eds., Cambridge University Press, https://doi.org/10.1017/CBO9781107415324.018..

Caldeira, K., and N. P. Myhrvold, 2013: Projections of the pace of warming following an abrupt increase in atmospheric carbon dioxide concentration. *Environ. Res. Lett.*, **8**, 034039, https://doi.org/10.1088/1748-9326/8/3/034039.

Carslaw, K. S., O. Boucher, D. Spracklen, G. Mann, J. Rae, S. Woodward, and M. Kulmala, 2010: A review of natural aerosol interactions and feedbacks within the Earth system. *Atmos. Chem. Phys.*, **10**, 1701–1737, https://doi.org/10.5194/acp-10-1701-2010.

——, and Coauthors, 2013: Large contribution of natural aerosols to uncertainty in indirect forcing. *Nature*, **503**, 67–71, https://doi.org/10.1038/nature12674.

——, L. A. Lee, L. A. Regayre, and J. S. Johnson, 2018: Climate models are uncertain, but we can do something about it. *Eos, Trans. Amer. Geophys. Union*, **99**, https://doi.org/10.1029/2018EO093757.

Ceppi, P., and J. M. Gregory, 2019: A refined model for the Earth's global energy balance. *Climate Dyn.*, **53**, 4781–4797, https://doi.org/10.1007/s00382-019-04825-x.

Chan, D., and P. Huybers, 2019: Systematic differences in bucket sea surface temperature measurements among nations identified using a linear-mixed-effect method. *J. Climate*, **32**, 2569–2589, https://doi.org/10.1175/JCLI-D-18-0562.1.

——, and ——, 2021: Correcting observational biases in sea surface temperature observations removes anomalous warmth during World War II. *J. Climate*, **34**, 4585–4602, https://doi.org/10.1175/JCLI-D-20-0907.1.

——, E. C. Kent, D. I. Berry, and P. Huybers, 2019: Correcting datasets leads to more homogeneous early-twentieth-century sea surface warming. *Nature*, **571**, 393–397, https://doi.org/10.1038/s41586-019-1349-2.

Charlson, R., S. Schwartz, J. Hales, R. Cess, J. J. A. Coakley, J. Hansen, and D. Hoffman, 1992: Climate forcing by anthropogenic aerosols. *Science*, **255**, 423–430, https://doi.org/10.1126/science.255.5043.423.

Cheng, L., K. E. Trenberth, J. Fasullo, T. Boyer, J. Abraham, and J. Zhu, 2017: Improved estimates of ocean heat content from 1960 to 2015. *Sci. Adv.*, **3**, e1601545, https://doi.org/10.1126/sciadv.1601545.

Chylek, P., and J. Wong, 1995: Effects of absorbing aerosols on the global radiation budget. *Geophys. Res. Lett.*, **22**, 929–931, https://doi.org/10.1029/95GL00800.

——, T. J. Vogelsang, J. D. Klett, N. Hengartner, D. Higdon, G. Lesins, and M. K. Dubey, 2016: Indirect aerosol effect increases CMIP5 models' projected Arctic warming. *J. Climate*, **29**, 1417–1428, https://doi.org/10.1175/JCLI-D-15-0362.1.

——, C. Folland, J. D. Klett, and M. K. Dubey, 2020: CMIP5 climate models overestimate cooling by volcanic aerosols. *Geophys. Res. Lett.*, **47**, e2020GL087047, https://doi.org/10.1029/2020GL087047.

Coats, S., and K. Karnauskas, 2017: Are simulated and observed twentieth century tropical Pacific sea surface temperature trends significant relative to internal variability? *Geophys. Res. Lett.*, **44**, 9928–9937, https://doi.org/10.1002/2017GL074622.

Cowtan, K., and R. Way, 2014: Coverage bias in the HadCRUT4 temperature series and its impact on recent temperature trends. *Quart. J. Roy. Meteor. Soc.*, **140**, 1935–1944, https://doi.org/10.1002/qj.2297.

——, and Coauthors, 2015: Robust comparison of climate models with observations using blended land air and ocean sea surface temperatures. *Geophys. Res. Lett.*, **42**, 6526–6534, https://doi.org/10.1002/2015GL064888.

——, R. Rohde, and Z. Hausfather, 2018: Evaluating biases in sea surface temperature records using coastal weather stations. *Quart. J. Roy. Meteor. Soc.*, **144**, 670–681, https://doi.org/10.1002/qj.3235.

Cummins, D. P., D. B. Stephenson, and P. A. Stott, 2020: Optimal estimation of stochastic energy balance model parameters. *J. Climate*, **33**, 7909–7926, https://doi.org/10.1175/JCLI-D-19-0589.1.

Davis, L. L., D. W. Thompson, J. J. Kennedy, and E. C. Kent, 2019: The importance of unresolved biases in twentieth-century sea surface temperature observations. *Bull. Amer. Meteor. Soc.*, **100**, 621–629, https://doi.org/10.1175/BAMS-D-18-0104.1.

Dong, Y., C. Proistosescu, K. C. Armour, and D. S. Battisti, 2019: Attributing historical and future evolution of radiative feedbacks to regional warming patterns using a Green's function approach: The preeminence of the western Pacific. *J. Climate*, **32**, 5471–5491, https://doi.org/10.1175/JCLI-D-18-0843.1.

Dudok de Wit, T., G. Kopp, C. Froehlich, and M. Schoell, 2017: Methodology to create a new total solar irradiance record: Making a composite out of multiple data records. *Geophys. Res. Lett.*, **44**, 1196–1203, https://doi.org/10.1002/2016GL071866.

Etminan, M., G. Myhre, E. J. Highwood, and K. P. Shine, 2016: Radiative forcing of carbon dioxide, methane, and nitrous oxide: A significant revision of the methane radiative forcing. *Geophys. Res. Lett.*, **43**, 12 614–12 623, https://doi.org/10.1002/2016GL071930.

Feingold, G., A. McComiskey, T. Yamaguchi, J. S. Johnson, K. S. Carslaw, and K. S. Schmidt, 2016: New approaches to quantifying aerosol influence on the cloud radiative effect. *Proc. Natl. Acad. Sci. USA*, **113**, 5812–5819, https://doi.org/10.1073/pnas.1514035112.

Feldstein, S. B., 2000: The timescale, power spectra, and climate noise properties of teleconnection patterns. *J. Climate*, **13**, 4430–4440, https://doi.org/10.1175/1520-0442(2000)013<4430:TTPSAC>2.0.CO;2.

Fiedler, S., and Coauthors, 2019: Anthropogenic aerosol forcing—Insights from multiple estimates from aerosol-climate models with reduced complexity. *Atmos. Chem. Phys.*, **19**, 6821–6841, https://doi.org/10.5194/acp-19-6821-2019.

Folland, C. K., O. Boucher, A. Colman, and D. E. Parker, 2018: Causes of irregularities in trends of global mean surface temperature since the late 19th century. *Sci. Adv.*, **4**, eaao5297, https://doi.org/10.1126/sciadv.aao5297.

Forest, C. E., 2018: Inferred net aerosol forcing based on historical climate changes: A review. *Curr. Climate Change Rep.*, **4**, 11–22, https://doi.org/10.1007/s40641-018-0085-2.

——, P. H. Stone, A. P. Sokolov, M. R. Allen, and M. D. Webster, 2002: Quantifying uncertainties in climate system properties with the use of recent climate observations. *Science*, **295**, 113–117, https://doi.org/10.1126/science.1064419.

——, ——, and ——, 2006: Estimated PDFs of climate system properties including natural and anthropogenic forcings. *Geophys. Res. Lett.*, **33**, L01705, https://doi.org/10.1029/2005GL023977.

——, ——, and ——, 2008: Constraining climate model parameters from observed 20th century changes. *Tellus*, **60A**, 911–920, https://doi.org/10.1111/j.1600-0870.2008.00346.x.

Forster, P. M., 2016: Inference of climate sensitivity from analysis of Earth's energy budget. *Annu. Rev. Earth Planet. Sci.*, **44**, 85–106, https://doi.org/10.1146/annurev-earth-060614-105156.

Frame, D., B. Booth, J. Kettleborough, D. Stainforth, J. Gregory, M. Collins, and M. Allen, 2005: Constraining climate forecasts: The role of prior assumptions. *Geophys. Res. Lett.*, **32**, L09702, https://doi.org/10.1029/2004GL022241.

Frankignoul, C., and K. Hasselmann, 1977: Stochastic climate models, Part II: Application to sea-surface temperature variability and thermocline variability. *Tellus*, **29**, 289–305, https://doi.org/10.3402/tellusa.v29i4.11362.

Gebbie, G., and P. Huybers, 2019: The Little Ice Age and 20th century deep Pacific cooling. *Science*, **363**, 70–74, https://doi.org/10.1126/science.aar8413.

Geoffroy, O., D. Saint-Martin, D. J. L. Olivié, A. Voldoire, G. Bellon, and S. Tyteca, 2013: Transient climate response in a two-layer energy-balance model. Part I: Analytical solution and parameter calibration using CMIP5 AOGCM experiments. *J. Climate*, **26**, 1841–1857, https://doi.org/10.1175/JCLI-D-12-00195.1.

Gettelman, A., 2015: Putting the clouds back in aerosol–cloud interactions. *Atmos. Chem. Phys.*, **15**, 12 397–12 411, https://doi.org/10.5194/acp-15-12397-2015.

——, and S. C. Sherwood, 2016: Processes responsible for cloud feedback. *Curr. Climate Change Rep.*, **2**, 179–189, https://doi.org/10.1007/s40641-016-0052-8.

Golaz, J.-C., and Coauthors, 2019: The DOE E3SM coupled model version 1: Overview and evaluation at standard resolution. *J. Adv. Model. Earth Syst.*, **11**, 2089–2129, https://doi.org/10.1029/2018MS001603.

Gregory, J. M., T. Andrews, P. Good, T. Mauritsen, and P. Forster, 2016: Small global-mean cooling due to volcanic radiative forcing. *Climate Dyn.*, **47**, 3979–3991, https://doi.org/10.1007/s00382-016-3055-1.

Hansen, J., and Coauthors, 2005: Earth's energy imbalance: Confirmation and implications. *Science*, **308**, 1431–1435, https://doi.org/10.1126/science.1110252.

Hasselmann, K., R. Sausen, E. Maier-Reimer, and R. Voss, 1993: On the cold start problem in transient simulations with coupled atmosphere–ocean models. *Climate Dyn.*, **9**, 53–61, https://doi.org/10.1007/BF00210008.

Hastings, W., 1970: Monte Carlo sampling methods using Markov chains and their application. *Biometrika*, **57**, 97–109, https://doi.org/10.1093/biomet/57.1.97.

Hauglustaine, D. A., Y. Balkanski, and M. Schulz, 2014: A global model simulation of present and future nitrate aerosols and their direct radiative forcing of climate. *Atmos. Chem. Phys.*, **14**, 11 031–11 063, https://doi.org/10.5194/acp-14-11031-2014.

Haustein, K., and Coauthors, 2019: A limited role for unforced internal variability in twentieth-century warming. *J. Climate*, **32**, 4893–4917, https://doi.org/10.1175/JCLI-D-18-0555.1.

Hegerl, G. C., T. J. Crowley, W. T. Hyde, and D. J. Frame, 2006: Climate sensitivity constrained by temperature reconstructions over the past seven centuries. *Nature*, **440**, 1029–1032, https://doi.org/10.1038/nature04679.

——, S. Brönnimann, A. Schurer, and T. Cowan, 2018: The early 20th century warming: Anomalies, causes, and consequences. *Wiley Interdiscip. Rev.: Climate Change*, **9**, e522, https://doi.org/10.1002/wcc.522.

Held, I. M., 2005: The gap between simulation and understanding in climate modeling. *Bull. Amer. Meteor. Soc.*, **86**, 1609–1614, https://doi.org/10.1175/BAMS-86-11-1609.

——, M. Winton, K. Takahashi, T. Delworth, F. Zeng, and G. K. Vallis, 2010: Probing the fast and slow components of global warming by returning abruptly to preindustrial forcing. *J. Climate*, **23**, 2418–2427, https://doi.org/10.1175/2009JCLI3466.1.

Hoesly, R. M., and Coauthors, 2018: Historical (1750–2014) anthropogenic emissions of reactive gases and aerosols from the Community Emissions Data System (CEDS). *Geosci. Model Dev.*, **11**, 369–408, https://doi.org/10.5194/gmd-11-369-2018.

Hoskins, B., 1983: Dynamical processes in the atmosphere and the use of models. *Quart. J. Roy. Meteor. Soc.*, **109** (459), 1–21, https://doi.org/10.1002/qj.49710945902.

Johansson, D. J., B. C. O. Neill, C. Tebaldi, and O. Häggström, 2015: Equilibrium climate sensitivity in light of observations over the warming hiatus. *Nat. Climate Change*, **5**, 449–453, https://doi.org/10.1038/nclimate2573.

Karl, T. R., and Coauthors, 2015: Possible artifacts of data biases in the recent global surface warming hiatus. *Science*, **348**, 1469–1472, https://doi.org/10.1126/science.aaa5632.

Kay, J. E., and Coauthors, 2015: The Community Earth System Model (CESM) large ensemble project: A community resource for studying climate change in the presence of internal climate variability. *Bull. Amer. Meteor. Soc.*, **96**, 1333–1349, https://doi.org/10.1175/BAMS-D-13-00255.1.

Kiehl, J. T., 2007: Twentieth century climate model response and climate sensitivity. *Geophys. Res. Lett.*, **34**, L22710, https://doi.org/10.1029/2007GL031383.

Knutti, R., T. F. Stocker, F. Joos, and G.-K. Plattner, 2002: Constraints on radiative forcing and future climate change from observations and climate model ensembles. *Nature*, **416**, 719–723, https://doi.org/10.1038/416719a.

——, M. A. Rugenstein, and G. C. Hegerl, 2017: Beyond equilibrium climate sensitivity. *Nat. Geosci.*, **10**, 727–736, https://doi.org/10.1038/ngeo3017.

Kretzschmar, J., M. Salzmann, J. Mülmenstädt, O. Boucher, and J. Quaas, 2017: Comment on rethinking the lower bound on aerosol radiative forcing. *J. Climate*, **30**, 6579–6584, https://doi.org/10.1175/JCLI-D-16-0668.1.

Laepple, T., and P. Huybers, 2014: Ocean surface temperature variability: Large model-data differences at decadal and longer periods. *Proc. Natl. Acad. Sci. USA*, **111**, 16 682–16 687, https://doi.org/10.1073/pnas.1412077111.

Leach, N. J., and Coauthors, 2021: FaIRv2.0.0: A generalized impulse response model for climate uncertainty and future scenario exploration. *Geosci. Model Dev.*, **14**, 3007–3036, https://doi.org/10.5194/gmd-14-3007-2021.

Lee, L., C. Reddington, and K. Carslaw, 2016: On the relationship between aerosol model uncertainty and radiative forcing uncertainty. *Proc. Natl. Acad. Sci. USA*, **113**, 5820–5827, https://doi.org/10.1073/pnas.1507050113.

Lehner, F., A. P. Schurer, G. C. Hegerl, C. Deser, and T. L. Frölicher, 2016: The importance of ENSO phase during volcanic eruptions for detection and attribution. *Geophys. Res. Lett.*, **43**, 2851–2858, https://doi.org/10.1002/2016GL067935.

Libardoni, A. G., and C. E. Forest, 2011: Sensitivity of distributions of climate system properties to the surface temperature dataset. *Geophys. Res. Lett.*, **38**, L22705, https://doi.org/10.1029/2011GL049431.

——, and ——, 2013: Correction to sensitivity of distributions of climate system properties to the surface temperature data set. *Geophys. Res. Lett.*, **40**, 2309–2311, https://doi.org/10.1002/grl.50480.

Malavelle, F. F., and Coauthors, 2017: Strong constraints on aerosol–cloud interactions from volcanic eruptions. *Nature*, **546**, 485–491, https://doi.org/10.1038/nature22974.

Marvel, K., G. A. Schmidt, R. L. Miller, and L. S. Nazarenko, 2016: Implications for climate sensitivity from the response to individual forcings. *Nat. Climate Change*, **6**, 386–389, https://doi.org/10.1038/nclimate2888.

McCoy, D. T., S. M. Burrows, R. Wood, D. P. Grosvenor, S. M. Elliott, P. L. Ma, P. J. Rasch, and D. L. Hartmann, 2015: Natural aerosols explain seasonal and spatial patterns of Southern Ocean cloud albedo. *Sci. Adv.*, **1**, e1500157, https://doi.org/10.1126/sciadv.1500157.

Meinshausen, M., and Coauthors, 2011: The RCP greenhouse gas concentrations and their extensions from 1765 to 2300. *Climatic Change*, **109**, 213–241, https://doi.org/10.1007/s10584-011-0156-z.

Metropolis, N., A. Rosenbluth, M. Rosenbluth, A. Teller, and E. Teller, 1953: Equation of state calculations by fast computing machines. *J. Chem. Phys.*, **21**, 1087–1092, https://doi.org/10.1063/1.1699114.

Morice, C. P., J. J. Kennedy, N. A. Rayner, and P. D. Jones, 2012: Quantifying uncertainties in global and regional temperature change using an ensemble of observational estimates: The HadCRUT4 data set. *J. Geophys. Res.*, **117**, D08101, https://doi.org/10.1029/2011JD017187.

Murphy, D., S. Solomon, R. Portmann, K. Rosenlof, P. Forster, and T. Wong, 2009: An observationally based energy balance for the Earth since 1950. *J. Geophys. Res.*, **114**, D17107, https://doi.org/10.1029/2009JD012105.

Myhre, G., and Coauthors, 2013: Anthropogenic and natural radiative forcing. *Climate Change 2013: The Physical Science Basis*, T. F. Stocker et al., Eds., Cambridge University Press, 659–740, https://doi.org/10.1017/CBO9781107415324.018.

O'Rourke, P. R., and Coauthors, 2021: CEDS v_2021_04_21 release emission data. Zenodo, accessed 1 June 2021, https://doi.org/10.5281/zenodo.4741285.

Otto, A., and Coauthors, 2013: Energy budget constraints on climate response. *Nat. Geosci.*, **6**, 415–416, https://doi.org/10.1038/ngeo1836.

Padilla, L. E., G. K. Vallis, and C. W. Rowley, 2011: Probabilistic estimates of transient climate sensitivity subject to uncertainty in forcing and natural variability. *J. Climate*, **24**, 5521–5537, https://doi.org/10.1175/2011JCLI3989.1.

Parsons, L. A., M. K. Brennan, R. C. Wills, and C. Proistosescu, 2020: Magnitudes and spatial patterns of interdecadal temperature variability in CMIP6. *Geophys. Res. Lett.*, **47**, e2019GL086588, https://doi.org/10.1029/2019GL086588.

Penner, J., and Coauthors, 1994: Quantifying and minimizing uncertainty of climate forcing by anthropogenic aerosols. *Bull. Amer. Meteor. Soc.*, **75**, 375–400, https://doi.org/10.1175/1520-0477(1994)075<0375:QAMUOC>2.0.CO;2.

Persad, G. G., and K. Caldeira, 2019: Divergent global-scale temperature effects from identical aerosols emitted in different regions. *Nat. Commun.*, **9**, 3289, https://doi.org/10.1038/s41467-018-05838-6.

Pincus, R., P. M. Forster, and B. Stevens, 2016: The Radiative Forcing Model Intercomparison Project (RFMIP): Experimental protocol for CMIP6. *Geosci. Model Dev.*, **9**, 3447–3460, https://doi.org/10.5194/gmd-9-3447-2016.

Polvani, L., A. Clement, B. Medeiros, J. Benedict, and I. Simpson, 2017: When less is more: Opening the door to simpler climate models. *Eos, Trans. Amer. Geophys. Union*, **99**, 15–16, https://doi.org/10.1029/2017EO079417.

Proistosescu, C., and P. J. Huybers, 2017: Slow climate mode reconciles historical and model-based estimates of climate sensitivity. *Sci. Adv.*, **3**, e1602821, https://doi.org/10.1126/sciadv.1602821.

Rodhe, H., R. Charlson, and T. Anderson, 2000: Avoiding circular logic in climate modeling. *Climatic Change*, **44**, 419–422, https://doi.org/10.1023/A:1005536902789.

Samset, B. H., G. Myhre, and M. Schulz, 2014: Upward adjustment needed for aerosol radiative forcing uncertainty. *Nat. Climate Change*, **4**, 230–232, https://doi.org/10.1038/nclimate2170.

Schneider, T., and A. Neumaier, 2001: Algorithm 808: ARfit—A Matlab package for the estimation of parameters and eigenmodes of multivariate autoregressive models. *ACM Trans. Math. Software*, **27**, 58–65, https://doi.org/10.1145/382043.382316.

Schwartz, S., 2018: Unrealized global temperature increase: Implications of current uncertainties. *J. Geophys. Res. Atmos.*, **123**, 3462–3482, https://doi.org/10.1002/2017JD028121.

Seinfeld, J. H., and Coauthors, 2016: Improving our fundamental understanding of the role of aerosol–cloud interactions in the climate system. *Proc. Natl. Acad. Sci. USA*, **113**, 5781–5790, https://doi.org/10.1073/pnas.1514043113.

Sherwood, S., and Coauthors, 2020: An assessment of Earth's climate sensitivity using multiple lines of evidence. *Rev. Geophys.*, **58**, e2019RG000678, https://doi.org/10.1029/2019RG000678.

Skeie, R., T. Berntsen, M. Aldrin, M. Holden, and G. Myhre, 2014: A lower and more constrained estimate of climate sensitivity using updated observations and detailed radiative forcing time series. *Earth Syst. Dyn.*, **5**, 139–175, https://doi.org/10.5194/esd-5-139-2014.

——, ——, ——, ——, and ——, 2018: Climate sensitivity estimates—Sensitivity to radiative forcing time series and observational data. *Earth Syst. Dyn.*, **9**, 879–894, https://doi.org/10.5194/esd-9-879-2018.

Smith, C. J., and Coauthors, 2020: Effective radiative forcing and adjustments in CMIP6 models. *Atmos. Chem. Phys.*, **20**, 9591–9618, https://doi.org/10.5194/acp-20-9591-2020.

——, and Coauthors, 2021: Energy budget constraints on the time history of aerosol forcing and climate sensitivity. *J. Geophys. Res. Atmos.*, **126**, e2020JD033622, https://doi.org/10.1029/2020JD033622.

Smith, S., J. van Aardenne, Z. Klimont, R. Andres, A. Volke, and S. Delgado Arias, 2011: Anthropogenic sulfur dioxide emissions: 1850–2005. *Atmos. Chem. Phys.*, **11**, 1101–1116, https://doi.org/10.5194/acp-11-1101-2011.

Sokolov, A. P., C. E. Forest, and P. H. Stone, 2010: Sensitivity of climate change projections to uncertainties in the estimates of observed changes in deep-ocean heat content. *Climate Dyn.*, **34**, 735–745, https://doi.org/10.1007/s00382-009-0556-1.

Stevens, B., 2015: Rethinking the lower bound on aerosol radiative forcing. *J. Climate*, **28**, 4794–4819, https://doi.org/10.1175/JCLI-D-14-00656.1.

——, 2018: Reply to "Comments on 'Rethinking the lower bound on aerosol radiative forcing.'" *J. Climate*, **31**, 9413–9416, https://doi.org/10.1175/JCLI-D-18-0185.1.

——, and G. Feingold, 2009: Untangling aerosol effects on clouds and precipitation in a buffered system. *Nature*, **461**, 607–613, https://doi.org/10.1038/nature08281.

——, S. C. Sherwood, S. Bony, and M. J. Webb, 2016: Prospects for narrowing bounds on Earth's equilibrium climate sensitivity. *Earth's Future*, **4**, 512–522, https://doi.org/10.1002/2016EF000376.

Su, W., N. Loeb, G. Schuster, M. Chin, and F. Rose, 2013: Global all-sky shortwave direct radiative forcing of anthropogenic aerosols from combined satellite observations and GOCART simulations. *J. Geophys. Res. Atmos.*, **118**, 655–669, https://doi.org/10.1029/2012JD018294.

Taylor, K. E., V. Balaji, S. Hankin, M. Juckes, B. Lawrence, and S. Pascoe, 2011: CMIP5 data reference syntax (DRS) and controlled vocabularies. PCMDI, 14 pp., https://pcmdi.llnl.gov/mips/cmip5/docs/cmip5_data_reference_syntax_v1-02_marked.pdf.

Tsutsui, J., 2017: Quantification of temperature response to CO_2 forcing in atmosphere–ocean general circulation models. *Climatic Change*, **140**, 287–305, https://doi.org/10.1007/s10584-016-1832-9.

Twomey, S., 1977: Influence of pollution on the short-wave albedo of clouds. *J. Atmos. Sci.*, **34**, 1149–1152, https://doi.org/10.1175/1520-0469(1977)034<1149:TIOPOT>2.0.CO;2.

von Schuckmann, K., and Coauthors, 2020: Heat stored in the Earth system: Where does the energy go? *Earth Syst. Sci. Data*, **12**, 2013–2041, https://doi.org/10.5194/essd-12-2013-2020.

Vyushin, D., and P. Kushner, 2009: Power-law and long-memory characteristics of the atmospheric general circulation. *J. Climate*, **22**, 2890–2904, https://doi.org/10.1175/2008JCLI2528.1.

Wigley, T., and S. Raper, 1992: Implications for climate and sea level of revised IPCC emissions scenarios. *Nature*, **357**, 293–300, https://doi.org/10.1038/357293a0.

Zanna, L., S. Khatiwala, J. M. Gregory, J. Ison, and P. Heimbach, 2019: Global reconstruction of historical ocean heat storage and transport. *Proc. Natl. Acad. Sci. USA*, **116**, 1126–1131, https://doi.org/10.1073/pnas.1808838115.

Zhang, H.-M., and Coauthors, 2019: Release of NOAA global surface temperature (noaaglobaltemp) dataset version 5. *2019 Fall Meeting*, San Francisco, CA, Amer. Geophys. Union, Abstract GC51O-1097, https://agu.confex.com/agu/fm19/meetingapp.cgi/Paper/519861.

Zhang, S., and Coauthors, 2016: On the characteristics of aerosol indirect effect based on dynamic regimes in global climate models. *Atmos. Chem. Phys.*, **16**, 2765–2783, https://doi.org/10.5194/acp-16-2765-2016.

Zhao, M., and Coauthors, 2018: The GFDL global atmosphere and land model AM4.0/LM4.0: 1. Simulation characteristics with prescribed SSTs. *J. Adv. Model. Earth Syst.*, **10**, 691–734, https://doi.org/10.1002/2017MS001208.

Zhou, C., M. D. Zelinka, and S. A. Klein, 2016: Impact of decadal cloud variations on the Earth's energy budget. *Nat. Geosci.*, **9**, 871–874, https://doi.org/10.1038/ngeo2828.